Moving Targets Imaging by SVD of a Space-Velocity MIMO Radar Data Driven Matrix

Liliana Borcea and Josselin Garnier

***Abstract*—We introduce a method for Multiple Input Multiple Output (MIMO) radar imaging of moving targets in a strongly reflecting, complex stationary scenery (clutter). The radar system has fixed nearby antennas that play the dual role of sources and receivers. It gathers data either by emitting probing pulses from one antenna at a time, or by sending from all the antennas non-coherent, possibly orthogonal, waveforms. We show how to obtain from the measurements an imaging function that depends on search position and velocity and is approximately separable in these variables, for a single moving target. For multiple moving targets in clutter, the imaging function is a sum of separable functions. By sampling this imaging function on a position-velocity grid we obtain an imaging matrix whose Singular Value Decomposition (SVD) allows the separation of the clutter and the targets moving at different velocities. The decomposition also leads directly to estimates of the locations and motion of the targets. The imaging method is designed to work in strong clutter, with unknown and possibly heterogeneous statistics. It does not require prior estimation of the covariance matrix of the clutter response or of its rank. We give an analysis of the imaging method and illustrate how it works with numerical simulations.**

***Index Terms*—Multiple input multiple output (MIMO) radar, moving target, clutter, imaging.**

I. INTRODUCTION

RADAR imaging is an important technology, with a long history and extensive literature [20], [42]. It involves clever engineering and signal processing [42] and it forms images with algorithms like filtered backprojection or matched filtering [17]. These are based on the linearization of the mapping between the unknown reflectivity of the illuminated region and the measured waves. Roughly, they sum coherently the data time traces synchronized with time delays corresponding to the imaging points. The most popular data acquisition setup is for monostatic, synthetic aperture radar (SAR), because it is simpler and does not require much coordination. We consider multiple input multiple output (MIMO) radar, which is receiving increasing attention due to its potential for improved target detection, discrimination and imaging [25], [30].

A large part of radar imaging is concerned with the detection, localization and tracking of moving targets in a stationary, strongly reflecting complex scene, called clutter [42]. Typically, moving targets are modeled by reflectivity functions with small (point-like) support in uniform, straight motion [18], [25], [29], [50]. This should be understood as a segment of a piecewise linear approximation of a general target trajectory, seen by the radar over the short duration of data gather. In our study we use such a model. Other models, like in inverse synthetic aperture radar (ISAR), allow target rotation [16], but require mathematical treatment specialized to the type of motion.

The effect of uniform motion of targets on SAR imaging, in the absence of clutter, is described in [28]: The targets are displaced in cross-range by an amount proportional to the range speed i.e., we have a Doppler shift leading to erroneous target placement. The images are also unfocussed, with the amount of blur depending on both the range and cross-range velocities. These facts have generated two general approaches for dealing with target motion: (1) Extract motion information directly from the data and (2) Work with formed images or track the targets via optimization, while forming images.

The oldest approach in the first category uses moving target indicator radars, which detect Doppler shifts in SAR data and subtract approximately the clutter returns. Examples are displaced phased center antenna (DPCA) radars and improvements, like notching techniques [42]. These impose constraints on antenna motion, they require accurate phase synchronization and may not work well for all moving targets. Newer approaches decompose processed SAR data into low-rank (clutter) and sparse (target) parts [6] or they use tensor decompositions based on sub-aperture data segmentations [35], [49]. These have not been tested in very strong clutter.

Examples of approaches in the second category are autofocus and optimization methods. Autofocus detects moving targets in formed images, by seeking to estimate and compensate phase errors that cause smearing [22]. Optimization with sparsity enforcing regularization has been used for imaging stationary and moving targets [13], [37], [44] and for compressed sensing i.e., imaging with undersampled data [2], [26], [32]. The sparsity is imposed directly on the reflectivity function or on the vector of coefficients in synthesis models with overcomplete dictionaries of position-velocity atoms and phase deviation errors. All these methods can produce images with very good resolution, but they

Received 4 May 2025; revised 17 August 2025, 27 October 2025, and 29 November 2025; accepted 1 December 2025. Date of publication 5 December 2025; date of current version 5 January 2026. This work was supported in part by the AFOSR under Award FA9550-22-1-0077 and in part by the Agence de l’Innovation de Défense (AID) via Centre Interdisciplinaire d’Études pour la Défense et la Sécurité (CIEDS) project PRODIPO. The associate editor coordinating the review of this article and approving it for publication was Dr. Jinyang Liang. *(Corresponding author: Liliana Borcea.)*

Liliana Borcea is with the Department of Applied Physics and Applied Mathematics, Columbia University, New York, NY 10027 USA (e-mail: lb3539@columbia.edu).

Josselin Garnier is with the CMAP at Ecole polytechnique, Institut Polytechnique de Paris, 91120 Palaiseau, France (e-mail: josselin.garnier@polytechnique.edu).

Digital Object Identifier 10.1109/TCI.2025.3640864

rely on having strong targets i.e., weak clutter. Multiple Signal Classification (MUSIC) is another "super-resolution" imaging approach [43] used mostly for stationary and sparse imaging scenes. It works if the signal/noise subspaces are well separated, but it lacks robustness with respect to noise [7], [34] and it is not equipped to deal with strong clutter and motion, aside from creating images frame by frame [52].

MIMO radar can improve the detection and resolution of imaging stationary and moving targets by using various transmission schemes and signal processing [15], [25], [36]. Unlike traditional radar systems that send coherent waveforms and generate focused beams, typical MIMO radar systems transmit omnidirectional and possibly orthogonal waveforms (e.g., Walsh-Hadamard codes [3]), that are resolved at the receivers by matched filters. In the case of MIMO radars with N coinciding source and receiver antennas, the matched filtering gives mathematically an active $N \times N$ array response matrix $\mathbf{R}(t)$, whose sth column contains the waves received at the array, generated by the sth antenna. This is our setting.

Strong stationary clutter poses a great challenge to imaging moving targets. The main technique for mitigating clutter is space-time adaptive processing (STAP) [10]. This estimates the covariance matrix of the clutter returns, which is typically low rank [11], and then uses it to produce a clutter filter applied to the received signals, with the purpose of increasing the moving targets signal-to-clutter-ratio (SCR).

There are multiple models of the statistics of clutter returns as functions of terrain, radar band and other parameters. The simplest models, especially for low bandwidth radar, assume a normal (Gaussian) clutter distribution. Other models propose log normal, Weibull and gamma distributions [1], [5], [40].

There are approximations of the rank of the covariance matrix of clutter returns (Brennan's rule) [11], [15]. A data-independent estimation of the clutter subspace, that takes into account the geometry of data acquisition, is in [15]. However, most STAP algorithms use training data to estimate the clutter covariance. The number of data samples for an adequate estimate is described in [39]. The training data is often limited in practice and violates the assumptions of target free, identically distributed and statistically independent samples, because in anticipation of heterogeneous clutter, the samples come from nearby range bins. Attempts to improve the estimation of clutter covariance include adaptive selection of training samples [38], [45] or sparse recovery STAP [53].

Compressed sensing methods that exploit the sparsity of clutter responses in the angle-Doppler plane have been used for STAP [15], [47], [50]. These methods can improve the estimation of the clutter covariance but they involve time consuming optimization and can be negatively affected by space-time discretization and subsequent grid misalignment [4]. Fixes of the latter, like the grid free atomic norm approach in [21], come at the expense of complexity, while the use of dense grids increases the computational burden. Tensor methods can mitigate somewhat this burden, as shown in [19].

Low-rank+sparse optimization, implemented via the Robust Principal Component Analysis (RPCA) procedure, has been used for imaging a few stationary or moving targets in clutter [41], [51]. The underlying assumption is that stationary clutter looks approximately the same in images formed from data segmented over sub-apertures. Therefore, it gives the low rank part of the matrix containing the stacked images, and it can be filtered out. RPCA is also used in [6], [35] for decomposing the data directly, prior to forming images. The decomposition is carried out in the fast and slow time domain, using a "normal move-out (NMO)" transformation. This nearly straightens the hyperbolic profile of the arrivals from clutter, thus making them low-rank. Both RPCA approaches rely on having strong targets (e.g., $\mathrm{SCR} > -3$ dB [51]). They also require careful segmentation of the data over sub-apertures, so that the clutter contribution is indeed low-rank and it is not confused with the signals from targets of interest [6], [35].

Typically, tensor-based MIMO radar imaging methods in clutter assume that the MIMO radar moves on a flight track parametrized by the slow time. Therefore, they use more data than assumed in this paper, where the MIMO radar is stationary. Tensor methods are based on higher-order singular value decompositions (HOSVD) and are complementary to STAP, because they use training data to estimate the clutter covariance matrix and then remove it via projection [12], [27], [48]. Without clutter, the data are modeled by sums of rank-one tensors, each corresponding to a moving target. These tensors can then be determined approximately by CANDECOMP/PARAFAC decompositions [48].

Our contribution: We introduce and analyze a novel approach to imaging from the $N \times N$ array response matrix $\mathbf{R}(t)$ gathered by a stationary MIMO radar system with N nearby source/receiver antennas, as explained above. We show how to map $\mathbf{R}(t)$ to an imaging function $I(\mathbf{y}, \mathbf{u})$ of the search position $\mathbf{y}$ and velocity $\mathbf{u}$, that is approximated by a sum of separable functions in $\mathbf{y}$ and $\mathbf{u}$. Separability is important, because by sampling $I(\mathbf{y}, \mathbf{u})$ on a position-velocity search grid, we obtain a "space-velocity imaging matrix" whose SVD can separate the contributions of moving targets from clutter.

We explain how to subtract the clutter response, separate the moving targets based on their velocity and then image them. We also obtain a resolution analysis for both the velocity estimation and target localization.

Our method complements the existing ones because:

1) It works in very strong clutter (low SCR). It gives automatically the locations and velocities of the targets.
2) It is not sensitive to the statistics of clutter, and therefore it can handle clutter distribution changes in the imaging region (heterogeneous clutter).
3) Unlike STAP, it does not require estimation of the covariance of clutter returns or its rank from training data.
4) It is less complex than tensor methods: Aside from needing training data to remove clutter, like in STAP, tensor methods involve HOSVD or CANDECOMP/PARAFAC decompositions obtained via iterative optimization.
5) It is less complex than low-rank+sparse methods which have not been tested in very strong clutter and involve delicate data processing and iterative optimization.

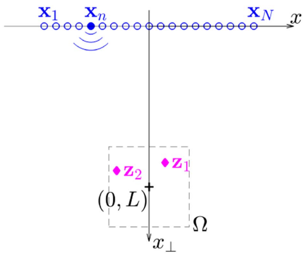

Fig. 1. Setup: Linear array of antennas, shown in blue, at $\mathbf{x}_n = (x_n, 0)$, $n = 1, \ldots, N$, is centered at $\mathbf{0} = (0, 0)$. The imaging region Ω is centered at $(0, L)$ and contains targets shown in red. There may be several targets and the drawing is not to scale. The diameter of Ω is assumed $\ll L$.

6) $I(\mathbf{y}, \mathbf{u})$ is given by matched filtering and summation over selected (source-receiver) antenna pairs. There is no iterative optimization and the SVD analysis can be made efficient by windowing in the search velocity and computing just a few leading singular values and vectors.

Outline: The paper is organized as follows: We give in Section II the setup and introduce in Section III the imaging function $I(\mathbf{y}, \mathbf{u})$. A resolution analysis of this imaging function is in Section IV, for the case of a single moving target. The technical details of the analysis are in Appendix A. The imaging algorithm described in Section V applies to multiple targets moving through clutter. We assess its performance with numerical simulations in Section VI. These simulations include a comparison with the STAP clutter cancellation approach. When an accurate estimate of the clutter covariance can be obtained from many independent, identically distributed and target-free training data samples, our method and STAP have similar performance. Our objective is to get an image without such training data, in which case STAP cannot be applied. We end with a brief summary in Section VII.

II. SETUP

Our methodology works in three dimensions, but to introduce the ideas, it suffices to consider two dimensions. The MIMO radar consists of a linear array of antennas separated by the distance Δa, and located at

$$\mathbf{x}_n = (x_n, 0), \qquad x_n = (n - N/2)\Delta a, \;\; n = 1, \ldots, N. \tag{1}$$

The aperture of the array is $a = N\Delta a$ and we use a system of coordinates $\mathbf{x} = (x, x_\perp)$ centered in the middle of the array, with range axis $x_\perp$ orthogonal to the array and cross-range axis x along the array (see Fig. 1).

The data acquisition is done in N steps. Each step corresponds to a signal emission from an antenna and the interval between the emissions is $\Delta\tau$. This interval is long enough to accomodate the arrival of the generated wave returns from the imaging region. More explicitly, at the sth step, the source at $\mathbf{x}_s$ emits the signal $f(t - T_s)$, delayed by $T_s = (s - N/2)\Delta\tau$. The wave returns are denoted by $R_{r,s}(t)$ and they are recorded by all the antennas indexed by $r = 1, \ldots, N$. This gives the sth column of the array response matrix $\mathbf{R}(t)$, which is filled step by step, using all the sources.

As explained in the introduction, the response matrix $\mathbf{R}(t)$ can also be obtained via signal processing, in the case of MIMO radars that emit non-coherent, typically orthogonal waveforms. The procedure is explained for example in [15, Section 6.3.1], where the entries of $\mathbf{R}(t)$ are determined using the transmitted waveforms as matched filters at the receivers.

While it is possible to use chirped signals, we assume that

$$f(t) = e^{-i\omega_o t} B\varphi(Bt) + \text{ c.c.} \tag{2}$$

is a pulse, modeled by an envelope function φ of dimensionless argument and compact support, modulated at the carrier frequency ω_o. The bandwidth of the pulse is quantified by B and "c.c." denotes the complex conjugate.

Scaling regime and model of the imaging scene: There are four important length scales in the problem: The range scale L, which quantifies the distance from the array to the imaging scene, the array aperture a, the carrier wavelength λ_o, and the length (proportional to the duration) of the pulse c/B, where c is the constant reference wave speed. The relations between these length scales determine how well we can image. We consider throughout a typical long range and high frequency regime, described by the relations

$$L \gg a \gg \lambda_o, \quad (a/L)^2 \ll B/\omega_o \ll 1. \tag{3}$$

The imaging scene lies in the domain Ω with diameter $\ll L$. It contains an arbitrary number M of moving targets and it is modeled by the reflectivity function

$$\rho(t, \mathbf{x}) = \sum_{j=1}^{M} \rho_j(\mathbf{x} - \mathbf{v}_j t) + \gamma(\mathbf{x}), \tag{4}$$

where $\gamma(\mathbf{x})$ is the reflectivity of the complex (cluttered) stationary scenery. The jth moving target has the reflectivity $\rho_j(\mathbf{x})$ and velocity $\mathbf{v}_j$. As stated in the introduction, the uniform motion model (4) is typical in the radar literature [18], [25], [29], [50]. It captures a segment of a piecewise linear approximation of more general target trajectories, observed over the brief duration of the measurement of $\mathbf{R}(t)$. In the numerical simulations we also consider targets with an acceleration, in order to showcase the robustness of the imaging method to deviations of the reflectivity model. We also give a bound on the magnitude of the acceleration for which the robustness holds.

We are interested in the case of strong clutter returns, where $\gamma(\mathbf{x})$ models numerous stationary scatterers whose cumulative effect overwhelms the reflections from the M moving targets. By design, our methodology introduced below is independent on the statistics of clutter i.e., the distribution of the locations and reflectivities of the stationary scatterers. In particular, the statistics of the locations may be homogeneous or heterogenous, with or without correlation properties.

Data model: We use, as is usual in radar, the single scattering (Born) approximation of the waves reaching the receivers in the array. To keep the presentation simple, we assume that the velocities of the targets are much smaller than the wave speed and we also use the stop-and-go approximation [17], [20]. The model of the response matrix is

$$\begin{aligned} R_{r,s}(t) = &\int_{\mathbb{R}} \frac{d\omega}{2\pi}\, k^2(\omega) e^{-i\omega(t - T_s)} \widehat{f}(\omega) \int_{\mathbb{R}^2} d\mathbf{z}\, \rho(T_s, \mathbf{z}) \\ &\times \widehat{G}(\omega, \mathbf{z}, \mathbf{x}_r) \widehat{G}(\omega, \mathbf{z}, \mathbf{x}_s) + \mathcal{N}_{r,s}(t), \end{aligned} \tag{5}$$

for $r, s = 1, \ldots, N$, where $k(\omega) = \omega/c$ is the wavenumber at frequency ω and the hats denote the Fourier transform with respect to time t. The wave propagation between points in the support of the reflectivity and the antennas in the array is modeled by the (two-dimensional) Green's function

$$\widehat{G}(\omega, \mathbf{x}, \mathbf{z}) = \frac{i}{4} H_0^{(1)} \left[k(\omega)|\mathbf{z} - \mathbf{x}|\right] \approx \frac{e^{\frac{i\pi}{4} + ik(\omega)|\mathbf{x}-\mathbf{z}|}}{2\sqrt{2\pi k(\omega)|\mathbf{x} - \mathbf{z}|}},$$

where $H_0^{(1)}$ is the Hankel function of the first kind and order 0. The approximation holds in regime (3).

The first term (the integral) in the data model (5) contains the signals coming from the moving targets [first terms in (4)] and the stationary scenery (the clutter) $\gamma(\mathbf{x})$. The signals from $\gamma(\mathbf{x})$ are the "clutter noise". In the low SCR regime of interest, this noise overwhelms the signals from the moving targets. Its statistics depends on the model of clutter. The only property we use is that the clutter does not change in time over the short duration of the data gather.

The term $\mathcal{N}_{r,s}(t)$ in (5) models other types of noise (electronic noise or signals coming from unknown and uncontrolled sources). If this noise is additive and uncorrelated, which is the typical situation addressed in the literature, then it does not have a strong effect, because it is canceled out approximately in the sums that define our imaging function. We illustrate this with numerical simulations in section VI. For simplicity of the presentation, we neglect additive noise in the analysis.

More complicated "noise", due to neglected multiple scattering, needs special consideration. If the medium between the array and the imaging region Ω is homogeneous and the correction of the Born approximation in (5) is not too strong, the multiple scattering "noise" gives a perturbation of our space-velocity imaging matrix that can be filtered out via the SVD. Cumulative strong multiple scattering in a random medium through which the waves propagate from the antennas to the imaging region and back is another story, not addressed here. We refer to [8], [23] for imaging stationary targets through such media. To our knowledge, the imaging of moving targets in random media has not yet been properly addressed.

The imaging problem: Localize moving targets and estimate their velocity, using the measurements gathered in the array response matrix $\mathbf{R}(t)$, with entries approximated by (5).

III. SEPARABLE SPACE-VELOCITY IMAGING FUNCTION

The standard, matched filter, space-velocity imaging function is given by the coherent sum

$$I^{MF}(\mathbf{y}, \mathbf{u}) = \frac{1}{N^2} \sum_{r,s=1}^{N} \int_{\mathbb{R}} dt\, R_{r,s}(t) \overline{H_{r,s}(t - T_s; \mathbf{y}, \mathbf{u})}, \quad (6)$$

where the bar denotes the complex conjugate and the data are synchronized using the filter

$$H_{r,s}(t; \mathbf{y}, \mathbf{u}) = \int_{\mathbb{R}} \frac{d\omega}{2\pi}\, e^{-i\omega t} \widehat{f}(\omega) \widehat{G}(\omega, \mathbf{x}_r, \mathbf{y} + \mathbf{u}T_s) \times \widehat{G}(\omega, \mathbf{x}_s, \mathbf{y} + \mathbf{u}T_s). \quad (7)$$

In the regime described by the scaling relations (3), it is known that if there is no moving target, $I^{MF}(\mathbf{y}, \mathbf{u} = \mathbf{0})$ peaks at points $\mathbf{y}$ near the stationary targets, with resolution of the order $\lambda_o L/a$ in cross-range and c/B in range. If there are moving targets, the space $\mathbf{y}$ and velocity $\mathbf{u}$ variables get tangled up in the expression of (6) [see Eq. (12)], thus complicating imaging and the separation of the moving targets from clutter.

To understand the origin of the entanglement between the space and velocity variables, it is useful to examine the phase of the integrand in (6). We write it using the paraxial approximation [9] that applies to the regime (3) and we introduce the velocity scale $V = \Delta a/\Delta\tau$, which depends on the experimental setup. By changing the antenna separation Δa and the interval $\Delta\tau$, we can increase or decrease V, which affects the resolution of the imaging, as shown in the next section. In particular, we wish that the target velocities be at most order V. Recalling the data model (4)-(5) we have, for a search point $\mathbf{y} + \mathbf{u}T_s$, with $\mathbf{y} = (y, y_\perp)$ and velocity $\mathbf{u} = (u, u_\perp)$, and for a target at $\mathbf{z} + \mathbf{v}T_s$, with $\mathbf{z} = (z, z_\perp)$ and $\mathbf{v} = (v, v_\perp)$, the following phase

$$\begin{aligned}
&\sum_{j \in \{s,r\}} \left(|\mathbf{x}_j - \mathbf{z} - T_s\mathbf{v}| - |\mathbf{x}_j - \mathbf{y} - T_s\mathbf{u}|\right) \\
&\approx 2\left[z_\perp - y_\perp + \left(\frac{z^2}{2z_\perp} - \frac{y^2}{2y_\perp}\right)\right] \\
&\quad + 2x_s\left[\frac{v_\perp - u_\perp}{V} + \left(\frac{z}{z_\perp}\frac{v}{V} - \frac{y}{y_\perp}\frac{u}{V}\right)\right] \\
&\quad - (x_s + x_r)\left[\frac{z}{z_\perp} - \frac{y}{y_\perp}\right] \\
&\quad + x_s^2\left[\frac{1}{z_\perp} - \frac{1}{y_\perp} + \left(\frac{v^2}{z_\perp V^2} - \frac{u^2}{y_\perp V^2}\right)\right] \\
&\quad - x_s(x_s + x_r)\left[\frac{1}{z_\perp} - \frac{1}{y_\perp} + \left(\frac{v}{z_\perp V} - \frac{u}{y_\perp V}\right)\right] \\
&\quad + (x_s + x_r)^2 \frac{1}{2}\left[\frac{1}{z_\perp} - \frac{1}{y_\perp}\right].
\end{aligned} \quad (8)$$

Note that the square brackets in this equation are multiplied by factors that depend on the source location x_s and the mid-point $(x_s + x_r)/2$ between the source and receiver. Moreover, in our long range regime (3), each square bracket has a dominant term and a smaller one (at least for $|v|, |u| < V$) written in the round brackets. Each dominant term involves the location coordinates of the target or the velocity, but not a mixture of these. To keep these terms from mixing up in the image, instead of superposing the data over all sources and receivers as in (6), we should superpose over the locations x_s of the sources and the mid-points $(x_s + x_r)/2$.

We propose to sum over the sources at $x_s \in [-a/4, a/4]$ and receivers that give $x_s + x_r \in [-a/4, a/4]$. As illustrated in the left plot of Fig. 2, this corresponds to the largest parallelogram with sides along the lines of constant x_s and constant $x_s + x_r$, that fits within the square $[-a/2, a/2] \times [-a/2, a/2]$ determined by the support of all source-receiver pairs in the data

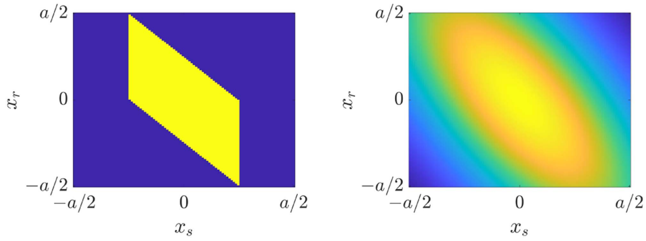

Fig. 2. Left: Selected pairs of source-receivers used to define $I(\mathbf{y},\mathbf{u})$: $x_s \in [-a/4, a/4]$ and $x_r \in [-a/4 - x_s, a/4 - x_s]$. Right: Gaussian apodization of the pairs $(x_s, x_r) \mapsto \exp[-2x_s^2/a^2 - 2(x_s + x_r)^2/a^2]$.

set. The space-velocity imaging function is

$$I(\mathbf{y},\mathbf{u}) = \frac{4}{N(N+2)} \sum_{s=\lfloor N/4 \rfloor}^{\lfloor 3N/4 \rfloor - 1} \sum_{r=\lfloor 3N/4 \rfloor - s}^{\lfloor 5N/4 \rfloor - s} \int_{\mathbb{R}} dt\, R_{r,s}(t) \times \overline{H_{r,s}(t - T_s; \mathbf{y}, \mathbf{u})}, \tag{9}$$

where the brackets $\lfloor \cdot \rfloor$ denote the integer part and we sum over the pairs (r, s) illustrated in the left plot of Fig. 2. To explain the choice of indexes in the sums, it is convenient to assume that N is an integer factor of 4, in order to avoid dealing with integer and fractional parts. For the source indexes we have

$$x_s = \left(s - \frac{N}{2}\right)\Delta a = \left(s - \frac{N}{2}\right)\frac{a}{N} \in \left[-\frac{a}{4}, \frac{a}{4}\right],$$

which gives $N/4 \leq s \leq 3N/4$, and for the receiver indexes

$$x_s + x_r = (s + r - N)\Delta a = (s + r - N)\frac{a}{N} \in \left[-\frac{a}{4}, \frac{a}{4}\right],$$

which gives $3N/4 - s \leq r \leq 5N/4 - s$. Since r must also satisfy $1 \leq r \leq N$, we restrict the upper bound on s to $3N/4 - 1$. Note that we have a total of $N/2 + 1$ terms in the sum over r and $N/2$ terms in the sum over s. In the analysis, we approximate the sums by integrals, so we introduce in (9) the normalization constant $[N/2(N/2 + 1)]^{-1} = 4/[N(N + 2)]$.

IV. RESOLUTION ANALYSIS

Since the data model is linear, to characterize the resolution of the space-velocity imaging function (9), it suffices to consider a single moving target in an empty imaging scene. The calculations are in Appendix A. They use a Gaussian apodization over the source-receiver pairs (see right plot in Fig. 2). The apodization is used just to obtain a simpler, explicit expression of $I(\mathbf{y},\mathbf{u})$. The separability of $I(\mathbf{y},\mathbf{u})$ and its resolution scales stated in Proposition 1 hold without the apodization, but the formulas are more complicated.

Proposition 1: Consider a single moving target with reflectivity $\rho(\mathbf{x} - \mathbf{v}t)$ in an otherwise empty imaging scene. If the cross-range components of the target velocity and the search velocity satisfy the relations

$$\frac{|v - u|}{V} \ll \frac{\lambda_o L}{a^2} \quad \text{and} \quad \frac{|u|}{V}, \ \frac{|v|}{V} = O(1), \tag{10}$$

then the space-velocity imaging function (9) has the expression

$$I(\mathbf{y},\mathbf{u}) \approx \frac{1}{64\pi^2 y_\perp^2} e^{-\frac{k_o^2 a^2}{2}\left(\frac{v_\perp - u_\perp}{V}\right)^2} \int_{\mathbb{R}^2} d\mathbf{z}\, \rho(\mathbf{z}) \times e^{-\frac{(k_o a)^2}{8}\left(\frac{z-y}{y_\perp}\right)^2} F\left[\frac{2}{c}\left(y_\perp - z_\perp + \frac{y^2}{2y_\perp} - \frac{z^2}{2z_\perp}\right)\right], \tag{11}$$

where $k_o = k(\omega_o) = 2\pi/\lambda_o$ and $F(t) = B\Phi(Bt)e^{-i\omega_o t} +$ c.c. is a signal with envelope $\Phi(h) = \int_{\mathbb{R}} dh'\, \overline{\varphi(h')}\varphi(h' + h)$.

The proposition says that $I(\mathbf{y},\mathbf{u})$ is approximately separable in the space and velocity variables when there is a single moving target. It is an imaging function because the integrand peaks at $\mathbf{y} = \mathbf{z} \in \text{supp}(\rho)$ (the support of ρ) and $u_\perp = v_\perp$. The resolution of the localization in cross-range is of order $\lambda_o L/a$ and in range it is of the order c/B. The range velocity resolution is of the order of $V\lambda_o/a$.

Under the same circumstances as in Proposition 1, the standard imaging function $I^{MF}(\mathbf{y},\mathbf{u})$ has the form

$$I^{MF}(\mathbf{y},\mathbf{u}) \approx \frac{1}{64\pi^2 y_\perp^2} e^{-\frac{k_o^2 a^2}{2}\left(2\frac{v_\perp - u_\perp}{V} - \frac{z-y}{y_\perp}\right)^2} \int_{\mathbb{R}^2} d\mathbf{z} \rho(\mathbf{z}) \times e^{-\frac{k_o^2 a^2}{2}\left(\frac{z-y}{y_\perp}\right)^2} F\left[\frac{2}{c}\left(y_\perp - z_\perp + \frac{y^2}{2y_\perp} - \frac{z^2}{2z_\perp}\right)\right]. \tag{12}$$

It is an imaging function because the integrand peaks at $\mathbf{y} = \mathbf{z} \in \text{supp}(\rho)$ and $u_\perp = v_\perp$, but it is not separable. A sum of such terms cannot be decomposed by SVD.

Since the velocity scale V is chosen by the user and it can be adapted by varying the emission interval $\Delta\tau$, the second condition in (10) can be fulfilled. The right hand side in the first condition of (10) is the inverse of the Fresnel number. This is of order one in a Fresnel diffraction regime and smaller than one in a Fraunhofer regime [9]. The larger the Fresnel number, the better guess of the cross-range velocity we need in (10). If the search velocity does not satisfy (10), then the more general formula of $I(\mathbf{y},\mathbf{u})$, given in Appendix A, shows that the statement of Proposition 1 should be modified, as follows: If the search velocity has cross-range component $u = 0$, then the imaging function peaks at $\mathbf{y} = \mathbf{z}$ and at

$$u_\perp = v_\perp + \frac{z}{z_\perp} v. \tag{13}$$

Since in our long range regime $|z| \ll y_\perp \sim L$, where the symbol $\sim$ stands for "has the same order as", the bias i.e., the last term in (13), is small.

Note that $I(\mathbf{y},\mathbf{u})$ cannot determine the cross-range component v of the target velocity $\mathbf{v}$. However, $\mathbf{v}$ can be determined using a second array, with aperture that is oblique with respect to the range direction. Recall that we are using less data than typical MIMO radar methods, where the array moves on some flight trajectory. By using a second array we can compute an imaging function analogous to $I(\mathbf{y},\mathbf{u})$ and determine the target velocity along the new range axis. Simple geometric calculations will then determine $\mathbf{v}$.

V. SELECTIVE IMAGING

The imaging function (9) is linear in the data matrix $\mathbf{R}(t)$, which sums the contribution of the clutter reflectivity $\gamma(\mathbf{x})$ and the M targets, according to (5). Thus, $I(\mathbf{y},\mathbf{u})$ is approximately a sum of M target terms of form (11), with $\rho(\mathbf{x})$ replaced by $\rho_j(\mathbf{x})$ and $v_\perp$ replaced by $v_{j,\perp}$, for $1 \leq j \leq M$, and the clutter term of the form (11), with $\rho(\mathbf{x})$ replaced by $\gamma(\mathbf{x})$ and $v_\perp$ replaced by

0. Here we show that we can determine each contribution using an SVD analysis of the imaging matrix $\mathbf{I}$ obtained by sampling $I(\mathbf{y}, \mathbf{u})$ on a position-velocity grid.

The position grid points $(\mathbf{y}_p)_{p=1}^P$ lie on a regular mesh of the imaging region $\Omega \subset \mathbb{R}^2$. A good choice of the grid steps is given by the resolution limits stated after Proposition 1.

Since we cannot determine the cross-range velocity in our scaling regime, we have a one-dimensional velocity search: We set $\mathbf{u} = (0, u_\perp)$ and search at $|u_\perp| \leq \mathrm{v}_{\max}$, where the velocity limit $\mathrm{v}_{\max}$ depends on the application. For example, in urban scenes, $\mathrm{v}_{\max} \approx 100\,\mathrm{km/hour}$. The search can be done by dividing the velocity interval in $2N_{u_\perp}$ subintervals

$$u_\perp \in [j\Delta u_\perp, (j+1)\Delta u_\perp], \quad -N_{u_\perp} \leq j \leq N_{u_\perp} - 1, \qquad (14)$$

where $\Delta u_\perp = \mathrm{v}_{\max}/N_{u_\perp}$ should be larger than the resolution limit $V\lambda_o/a$. The method selects only the targets with $u_\perp$ in such a search interval (the other targets are treated like clutter). There is a trade-off that dictates the choice of $\Delta u_\perp$: On one hand, if $\Delta u_\perp$ is large, we zoom out the image (determine more targets at once) and need fewer searches to cover the whole range of expected velocities. On the other hand, if $\Delta u_\perp$ is small, we zoom in a few targets and reduce the computational cost of the matrix $\mathbf{I}$ and its SVD, but we have more searches.

Let us focus attention on one search, in one of the intervals (14), denoted $[V_{\min}, V_{\max}]$, sampled uniformly at points $u_{\perp,q}$, in steps of order $V\lambda_o/a$. The $P \times Q$ imaging matrix is defined by $\mathbf{I} = (I(\mathbf{y}_p, \mathbf{u}_q))_{1 \leq p \leq P, 1 \leq q \leq Q}$, with $\mathbf{u}_q = (0, u_{\perp,q})$. Its SVD decomposition is

$$\mathbf{I} = \mathbf{\Gamma}\mathbf{\Sigma}\mathbf{\Theta}^\star, \qquad (15)$$

where the entries of the diagonal matrix $\mathbf{\Sigma}$ are the singular values, the columns of $\mathbf{\Gamma}$ are the left singular vectors and the columns of $\mathbf{\Theta}$ are the right singular vectors. The star denotes the complex conjugate and transpose.

To see what to expect, return briefly to the case of a single target and no clutter, where $I(\mathbf{y}, \mathbf{u})$ has the form (11). Then, the matrix $\mathbf{I}$ would have one large singular value, with associated left singular vector given, up to the normalization, by the sampling of

$$\frac{1}{y_\perp^2}\int_{\mathbb{R}^2} d\mathbf{z}\, \rho(\mathbf{z}) e^{-\frac{k_o^2 a^2}{2}\left(\frac{z-y}{y_\perp}\right)^2} F\left[\frac{2}{c}\left(y_\perp - z_\perp + \frac{y^2}{2y_\perp} - \frac{z^2}{2z_\perp}\right)\right]$$

at $(\mathbf{y}_p)_{p=1}^P$. The right singular vector would be given, up to the normalization, by the sampling of $e^{-\frac{k_o^2 a^2}{2}(\frac{v_\perp - u_\perp}{V})^2}$ on the velocity grid $(u_{\perp,q})_{q=1}^Q$. Note how the left singular vector gives the image of the target (peaks in $\mathrm{supp}(\rho)$), while the right singular vector peaks at the target velocity $v_\perp$. This result holds if $v_\perp \in [V_{\min}, V_{\max}]$. Otherwise, all the singular values of $\mathbf{I}$ would be negligible.

For the general model with M moving targets in clutter, there are three scenarios:

1) *The clutter is stronger than the moving targets and the M moving targets have different range velocity in $[V_{\min}, V_{\max}]$:* In this scenario, the largest singular value σ_1 corresponds to clutter and the leading left singular vector Γ_1, with rows corresponding to $(\mathbf{y}_p)_{p=1}^P$, contain the image of the stationary scene. The rows of the right singular vector Θ_1 correspond to the search velocity and we have a peak at $q \in \{1, \ldots, Q\}$ such that $\mathbf{u}_q \approx \mathbf{0}$. The next M significant singular values $(\sigma_{j+1})_{1 \leq j \leq M}$ correspond to the moving targets. The associated left singular vectors Γ_{j+1} give the image of the jth target i.e., they peak at the rows near its location. The right singular vectors Θ_{j+1} peak at the rows near the range velocity $v_{\perp,j}$. The remaining singular values are negligible and account for the errors of approximation of $I(\mathbf{y}, \mathbf{u})$.

2) *The clutter is stronger than the moving targets and m of these targets, with $m \leq M$, have the same range velocity (while the other targets have different range velocities):* In this scenario we expect large singular values σ_{j+1} for $j = 1, \ldots, M - m + 1$. There should be one singular value associated with the m targets and the right singular vector should peak near their range velocity. The left singular vector should peak at rows near the locations of these targets.

3) *The stationary scenery is weaker than the moving targets:* In this scenario the leading part of the spectrum corresponds to the moving targets. The results above hold, with σ_{j+1} replaced by σ_j, for $j = 1, \ldots, M$.

Note that our interpretation of the three scenarios assumes that the targets are separated by more than the resolution limit $\lambda_o L/a$ in cross-range and c/B in range. This ensures the orthogonality of the columns of $\mathbf{\Gamma}$. Similarly, the orthogonality of the columns of $\mathbf{\Theta}$ is ensured when the range velocities of the targets are separated by more than $V\lambda_o/a$. If this is not the case, then we may have a cluster of singular values and associated singular vectors, with components that are large (in magnitude) near the locations and velocities of the targets (see Appendix C for an illustration).

Note also that the expression (11) is the leading order term of the contribution of any target with velocity $\mathbf{v}$ that may be zero if the target is part of the stationary clutter. If the clutter is very strong i.e., we have many stationary targets, then the correction terms to the formula (11) start to play a role and we may see more than one leading singular value associated with it. This is not an issue because when searching for moving targets, we can just ignore the leading singular values corresponding to the right singular vectors that do not display a peak at search velocity $u_\perp$ away from 0.

The imaging process can be automated, in principle. It involves more than setting a threshold for selecting the significant singular values, because some of these may be due to artifacts induced by corrections to (11). The automation is feasible because the artifacts can be detected as shown in Appendix B. The idea is to analyze $I(\mathbf{y}, (0, u_\perp))$ at points $\mathbf{y}$ in a zoomed in domain. If the singular value corresponds to a target, the new left singular vector gives a zoomed version of the original image. If the image is quite different, the singular value corresponds to an artifact.

VI. Numerical Results

We use numerical simulations to illustrate the performance of the selective imaging approach described in section V and compare it with the STAP method carried out in an ideal setting where there are sufficient training data to get an accurate estimate of the covariance of clutter returns.

Setup: The numerical simulations use the data model (5) and additive noise. The setup is described by the normalized range and aperture scales $k_oL = 200$ and $k_oa = 60$, where $k_o = \omega_o/c_o$. The bandwidth is $B = \omega_o/10$. There are $N = 40$ antennas in the array. The velocity scale is $V = 1.5/(k_o\Delta\tau)$ where $\Delta\tau$ is the emission interval. The envelope of the emitted pulse in (2) has the Fourier transform

$$\widehat{\varphi}(w) = \exp(-4w^2)\mathbf{1}_{[-1,1]}(w), \tag{16}$$

where $\mathbf{1}_{[-1,1]}(w)$ is the indicator function of the interval $[-1, 1]$, equal to 1 if $|w| \leq 1$ and zero otherwise.

The imaging region is $\Omega = [-100, 100]/k_o \times [100, 300]/k_o$. Note that Ω is larger than assumed in the analysis, thus testing the limits of the paraxial approximation. The numerical results reported below show that the paraxial approximation is robust. The theoretical resolution limits in Proposition 1 are: $13/k_o$ in cross-range, $5/k_o$ in range, and $0.05V$ in range velocity.

The imaging function is computed with the formula (9). The hard cut-offs in this formula generate sinc-like lobes in the images. These are mitigated by the Gaussian apodization in the analysis that lead to Proposition 1. As explained there, the apodization does not change the separability of the imaging function or its resolution scales. Its sole purpose is to make the expression of $I(\mathbf{y}, \mathbf{u})$ explicit and easier to understand.

Computational complexity: The definition of the imaging function (9) and subsequently, of the imaging matrix $\mathbf{I}$, only involves summation and multiplication with the filter (7). Each column of $\mathbf{I}$ corresponds to a sample search speed $\mathbf{u}_q = (u, u_{\perp_q})$ and its computation is as efficient as that of standard radar image formation. The number of columns is given by $(V_{\max} - V_{\min})/(V\lambda_o/a)$. As explained in section V, we can reduce the computational cost of $\mathbf{I}$ by restricting the velocity search to smaller intervals. We can also window in the search location i.e., image in a subdomain of Ω. In addition to controlling the size of $\mathbf{I}$ by space-velocity windowing, we can use a truncated SVD i.e., compute just a few of the leading singular values and associated singular vectors. The method does not involve iterative optimization. Thus, its computational cost should compare favorably to approaches like compressed sensing or tensor methods, which use optimization, in addition to other delicate processing.

A. Clutter Model

The clutter reflectivity $\gamma(\mathbf{x})$ in the model (4) corresponds to many stationary, point-like scatterers randomly distributed in Ω. Our imaging method is insensitive to the statistics of clutter, but we show results for three models: • **Homogeneous clutter:** There are 1000 scatterers at independent, identically and uniformly distributed locations in Ω. Their reflectivities are modeled as random, with zero-mean normal distribution and standard deviation equal to a one tenth of the reflectivities of the moving targets. • **Heterogeneous clutter:** There are 1000 scatterers at locations that are independent and identically distributed with the non-uniform distribution in Ω with density proportional to $(k_ox_\perp/200)(k_ox + 100)/100$. • **Hyperuniform clutter:** There are 1024 scatterers at locations that form a hyperuniform cloud in Ω (more exactly we use a randomly perturbed square periodic lattice). This has long-range correlations that result in the suppression of density fluctuations over large distances [46].

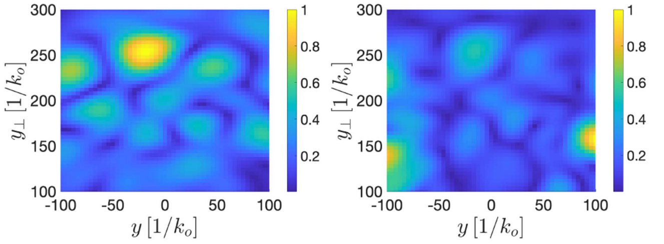

(a) Image from Γ_1 **(b) Image from Γ_2**

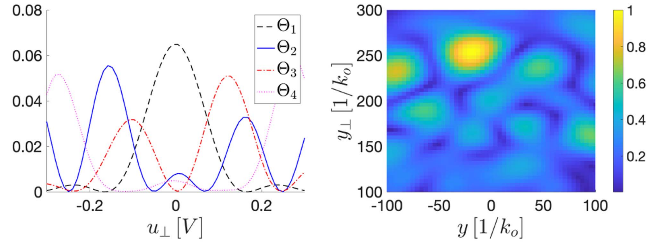

(c) Right singular vectors **(d) $|I(\mathbf{y}, \mathbf{0})|$**

Fig. 3. Results in homogeneous clutter, without moving target. Search velocity interval is $[-0.3, 0.3]V$ with step $0.01V$. The axes y and $y_\perp$ are in units $1/k_o$ and $u_\perp$ is in units V. The first four singular values $(\sigma_j)_{j=1}^4 = (5.0337, 0.3036, 0.1905, 0.0847) \times 10^5$. Plots (a) and (b) display the moduli of the first and second left singular vectors: $|\Gamma_1|$ and $|\Gamma_2|$. Plot (c) displays the square moduli of the first four right singular vectors: $|\Theta_1|^2, \ldots, |\Theta_4|^2$. Plot (d) displays $|I(\mathbf{y}, \mathbf{0})|$. The images (a)-(b)-(d) are normalized to maximal value 1 (our imaging method is qualitative as it plots a singular vector, whose norm is always 1).

We remark that for the three models, the density of clutter scatterers is large enough to make their image look like a speckle pattern [see Fig. 3(a) for an illustration]. Their random reflectivities are also strong enough to ensure a low SCR i.e., the images of the moving targets are masked by the speckle pattern (as shown in the figures). The SCR is defined by

$$SCR = 10\log_{10}\frac{\sum_{r,s}\int_{\mathbb{R}} dt\,|R^{\rho}_{r,s}(t)|^2}{\sum_{r,s}\int_{\mathbb{R}} dt\,|R^{\gamma}_{r,s}(t)|^2}\ \text{dB},$$

where the signal $R^{\rho}_{r,s}$ is generated by the moving target and $R^{\gamma}_{r,s}$ is generated by the stationary clutter.

The results in Fig. 3 are for homogeneous clutter. Note that the first right singular vector is maximal at $\mathbf{u} = \mathbf{0}$ [Fig. 3(c)] and the corresponding left singular vector Γ_1 gives an image of the speckle produced by the targets in clutter [Fig. 3(a)]. The latter is very close to the image $I(\mathbf{y}, \mathbf{0})$ plotted in Fig. 3(d). While the second singular value is considerably smaller than the first ($\sigma_2 = 0.0603\sigma_1$), one may wonder if it corresponds to a slowly moving target with velocity close to $-0.2V$ [which gives the maximum of the second right singular vector in Fig. 3(c)]. There is no moving target in this simulation, so what we see in Fig. 3(b)–(c) are the orthonormal singular vectors due to the corrections (the neglected higher order terms) of the formula in Proposition 1. These artifacts can be detected and ignored, as explained in section V and Appendix B.

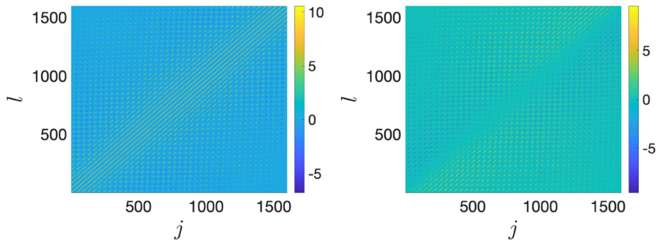

(a) Real part of C **(b) Imaginary part of C**

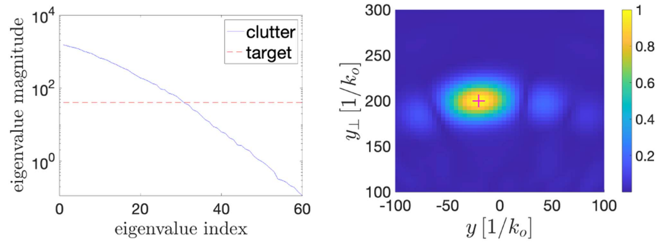

(c) Eigenvalues of C **(d) $|I(\mathbf{y},\mathbf{v})|$**

Fig. 4. STAP method: Plots (a)-(b) show the real and imaginary part of the empirical clutter covariance matrix $\mathbf{C} = (C_{jl})_{j,l=1}^{N^2}$, with $j = r' + (s'-1)N$ and $l = r + (s-1)N$, $N = 40$. Plot (c) gives the first 60 eigenvalues of $\mathbf{C}$, compared with the amplitude of the moving target. Plot (d) gives the image $|I(\mathbf{y},\mathbf{v})|$ (at the true $\mathbf{v}$) obtained in the same configuration as in Figure 5 but after applying the clutter filter to the data. The image is normalized to maximal value 1. The SCR is -10 dB.

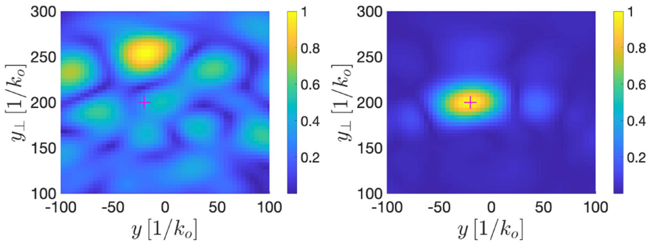

(a) Image from Γ_1 **(b) Image from Γ_2**

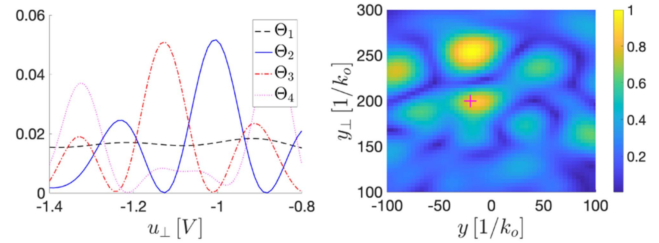

(c) Right singular vectors **(d) $|I(\mathbf{y},\mathbf{v})|$**

Fig. 5. Results in homogeneous clutter with one moving target. The target position at $t = 0$ is shown with a red cross. Its velocity is $\mathbf{v} = (0,-1)V$. The search velocity interval is $[-1.4,-0.8]V$, with step $0.01V$. The first four singular values are $(\sigma_j)_{j=1}^4 = (1.0052, 0.1298, 0.0304, 0.0198) \times 10^6$. The SCR is -9.8 dB. Plots (a) and (b) display $|\Gamma_1|$ and $|\Gamma_2|$. Plot (c) displays $|\Theta_1|^2,\ldots,|\Theta_4|^2$. Plot (d) displays $|I(\mathbf{y},\mathbf{v})|$ at the true $\mathbf{v}$. The images are normalized to maximal value 1.

B. One Moving Target in Clutter

Here we present results for a single moving target in stationary and clutter. We consider first homogeneous clutter, but test later the robustness of the method to heterogeneous and hyperuniform clutter. Most of the results are for the typical SAR model of a point target, but we include at the end of the section the results for an extended target.

In the first simulation (Figs. 4–5) the target moves through homogeneous clutter, on the trajectory $\mathbf{z} + \mathbf{v}t$, with velocity $\mathbf{v} = (0,-1)V$ in the range direction and $\mathbf{z} = (-20, 200)/k_o$. The target reflectivity is modeled by $\delta[\mathbf{x} - (\mathbf{z} + \mathbf{v}t)]$.

STAP comparison benchmark (Fig. 4): To assess the performance of our imaging method against the popular STAP approach [47], we show here results for an ideal STAP setting, where the covariance of the homogeneous clutter returns can be estimated accurately. To compute this covariance, we used $N_e = 100$ numerical experiments, carried out with independent and identically distributed realizations of the random scenery and without any moving target. During the e-the experiment a data cube $R^{(e)}_{r,s}(t)$ of size $N \times N \times N_t$ is recorded. Recall that N is the number of sources and receivers, while N_t is the number of time samples at Nyquist rate. The $N^2 \times N^2$ clutter covariance matrix $\mathbf{C}$, with entries denoted by $C_{(r',s'),(r,s)}$, for $r, r', s, s' = 1,\ldots,N$, is estimated by the empirical mean, as stated in [47, Section 2.4.2],

$$C_{(r',s'),(r,s)} = \frac{1}{N_e N_t}\sum_{t=1}^{N_t}\sum_{e=1}^{N_e} R^{(e)}_{r',s'}(t)\, R^{(e)}_{r,s}(t). \tag{17}$$

The illustration of $\mathbf{C}$ in Fig. 4(a)–(b) shows that the clutter response is highly structured. STAP uses $\mathbf{C}$ to filter out the clutter components from each time sample $(R_{r,s}(t))_{r,s=1}^N$ collected in a scene with both clutter and the moving target. Here the filter is the orthogonal projection onto the last $N^2 - 30$ eigenvectors of $\mathbf{C}$. The number 30 has been chosen by comparing the eigenvalues of $\mathbf{C}$ to the amplitude of the contribution of the moving target i.e., the scalar value such that a time sample from the moving target is a unitary N^2-vector multiplied by this scalar: As shown in Fig. 4(c), there are approximately 30 eigenvalues of $\mathbf{C}$ that are larger than the moving target amplitude. The corresponding 30 eigenvectors are well estimated from the first N_e experiments and, as a result, the image obtained with the filtered data gives a nice image of the moving target [see Fig. 4(d)].

Note that the STAP results shown here require a lot of preliminary data in order to learn the covariance matrix of the clutter response. We also used knowledge of the amplitude of the moving target response in order to extract it from the measurements, via proper filtering. The method proposed in the paper does not rely on knowing the covariance matrix of the clutter response and therefore, it does not require additional training data. It works just with the data collected once, in the presence of the moving targets, and it is robust with respect to the statistics of clutter, as shown later in this section.

Our imaging method (Fig. 5): We form the space-velocity imaging matrix using the search velocity $\mathbf{u} = (0, u_\perp)$, with $u_\perp$ sampling the interval $[-1.4,-0.8]V$, by step $0.01V$, and the search point $\mathbf{y}$ sampling the region $[-100/k_o, 100/k_o] \times [100/k_o, 300/k_o]$, on a 51×51 regular grid with step $4/k_o$.

The leading singular right and left vectors are due to the strong clutter. We know they are not due to a moving target with velocity in the search range, because the right singular vector Θ_1 does not have a clear peak [Fig 5(c)]. The random stationary scenery

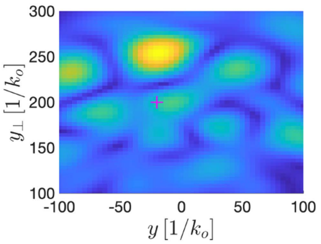

(a) Image from Γ_1 **(b) Image from Γ_2**

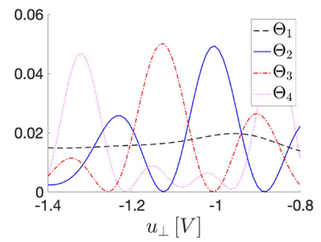

(c) Right singular vectors **(d) $|I(\mathbf{y},\mathbf{v})|$**

Fig. 6. Setup as in Fig. 5, but high $SCR = -3.8$ dB. Plots (a) and (b) display $|\Gamma_1|$ and $|\Gamma_2|$. Plot (c) displays $|\Theta_1|^2, \ldots, |\Theta_4|^2$. Plot (d) displays $|I(\mathbf{y},\mathbf{v})|$ at the true $\mathbf{v}$. The images are normalized to maximal value 1 and the colorbars are as in Fig. 5. The image in (d) is reasonable but noisy.

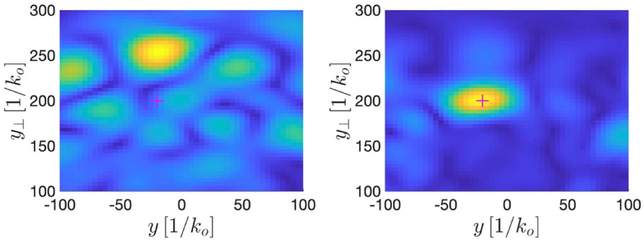

(a) Image from Γ_1 **(b) Image from Γ_2**

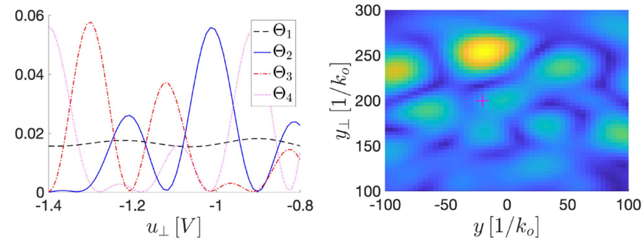

(c) Right singular vectors **(d) $|I(\mathbf{y},\mathbf{v})|$**

Fig. 7. Setup as in Fig. 5 but low $SCR = -21.9$ dB. Plots (a) and (b) display $|\Gamma_1|$ and $|\Gamma_2|$. Plot (c) displays $|\Theta_1|^2, \ldots, |\Theta_4|^2$. Plot (d) displays $|I(\mathbf{y},\mathbf{v})|$ at the true $\mathbf{v}$. Images are normalized to maximal value 1 and the colorbars are as in Fig. 5. Image given by our method (Fig. (b)) is still good.

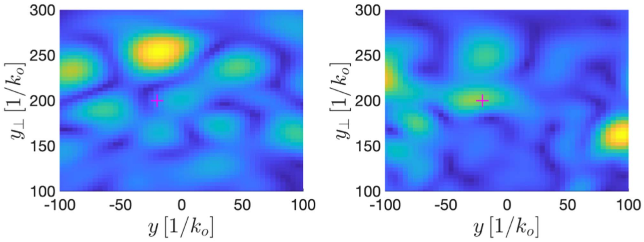

(a) Image from Γ_1 **(b) Image from Γ_2**

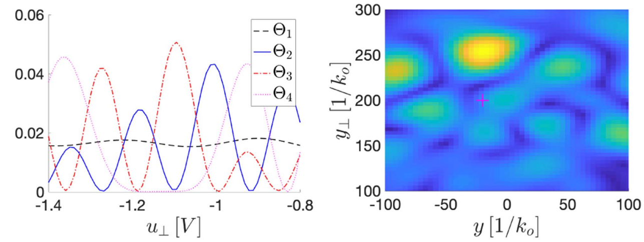

(c) Right singular vectors **(d) $|I(\mathbf{y},\mathbf{v})|$**

Fig. 8. Setup as in Fig. 5 but very low $SCR = -27.9$ dB. Plots (a) and (b) display $|\Gamma_1|$ and $|\Gamma_2|$. Plot (c) displays $|\Theta_1|^2, \ldots, |\Theta_4|^2$. Plot (d) displays $|I(\mathbf{y},\mathbf{v})|$ at the true $\mathbf{v}$. The images are normalized to maximal value 1 and the colorbars are as in Fig. 5. The image in Fig. (b) is now deteriorated.

is strong and thus the correction to the approximation of its contribution in Proposition 1 is stronger than the contribution of the moving target (observe that $\sigma_1 \gg \sigma_2$). The moving target gives the second singular value. The corresponding left singular vector Γ_2 contains its image, which peaks at the true target location $\mathbf{z} = (-20, 200)/k_o$ at $t = 0$ [Fig. 5(b)]. The right singular vector Θ_2 peaks at the true range velocity $v_\perp = -V$ [blue line in Fig. 5(c)]. Note that the image in Fig. 5(b) is as good as that in Fig. 3(d), obtained with the STAP approach, carried out in the ideal setting. However, Fig. 5(b) is obtained without needing to estimate the covariance of the clutter returns.

In Fig. 5(d) we plot $\big|I(\mathbf{y},\mathbf{u}=\mathbf{v})\big|$. Even though we use the true target velocity, the image shows a slightly misplaced moving target, due to the superposition with a blurry version of the strong stationary scenery. This illustrates the main finding in this paper: the SVD of the space-velocity imaging matrix can locate the moving target and separate it from stationary clutter more efficiently and accurately than matched filtering and an optimization search.

Robustness to clutter strength i.e., SCR (Figs. 6-8): The setup in Figs. 6-8 is the same as in Fig. 5, but the SCR varies from high to low. It becomes clear that the SVD approach can extract a moving target whose signal can be deeply buried into the one of the stationary scenery. Explicitly, the results are good for an SCR as low as -27 dB.

Robustness to clutter statistics (Figs. 9-10): We display results for heterogeneous and hyperuniform clutter, modeled as expained in Subsection VI-A. The imaging results shown in the plots (b)-(c) are basically the same as in homogeneous clutter (Fig. 5). This verifies that our method is independent of the statistics of clutter.

Robustness to non-uniform motion (Fig. 11): All the results above are for a target with constant velocity. Here we study the robustness of our method to the assumption of uniform motion, by considering a target with constant acceleration $\mathbf{g}$. The analysis of the imaging function for such a target is similar to that in Appendix A: When using the target position $\mathbf{z} + \mathbf{v}T_s + \mathbf{g}T_s^2/2$ in the data model, we get additional terms in the phase expansion (8). The dominant additional terms are of the form $x_s^2(x_s + x_r)g/(V^2 z_\perp)$. These are negligible if the acceleration satisfies $|\mathbf{g}| \ll 4V^2 L\lambda_o/a^3$. In Fig. 5 we consider a target with such an acceleration. Its velocity increases linearly

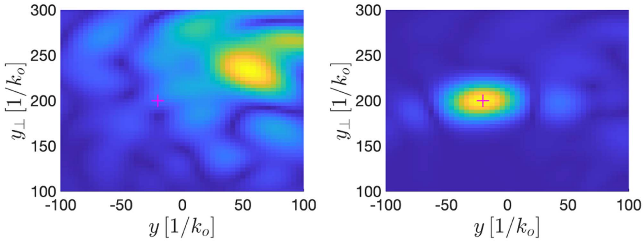

(a) Image from Γ_1 **(b) Image from Γ_2**

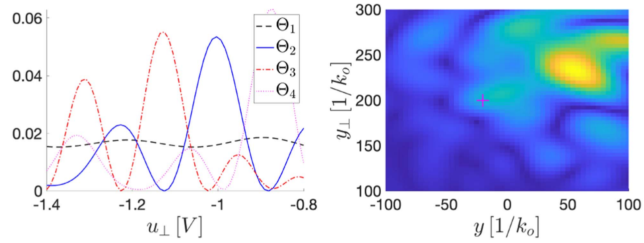

(c) Right singular vectors **(d) $|I(\mathbf{y},\mathbf{v})|$**

Fig. 9. Heterogeneous clutter: Setup as in Fig. 5, but the clutter has a strong spatial gradient. $SCR = -13.7$ dB. Plots (a) and (b) display $|\Gamma_1|$ and $|\Gamma_2|$. Plot (c) displays $|\Theta_1|^2, \ldots, |\Theta_4|^2$. Plot (d) displays $|I(\mathbf{y},\mathbf{v})|$ at the true $\mathbf{v}$. Images are normalized to maximal value 1 and the colorbars are as in Fig. 5.

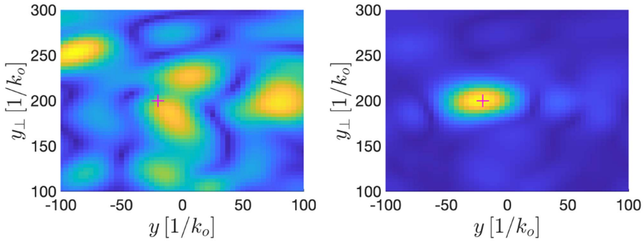

(a) Image from Γ_1 **(b) Image from Γ_2**

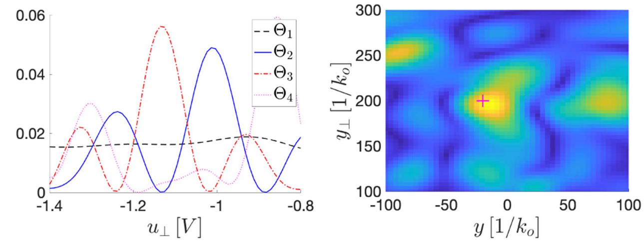

(c) Right singular vectors **(d) $|I(\mathbf{y},\mathbf{v})|$**

Fig. 10. Hyperuniform clutter: Setup as in Fig. 5, but the clutter is a strongly correlated cloud of point-like scatterers. Here $SCR = -9.8$ dB. Plots (a) and (b) display $|\Gamma_1|$ and $|\Gamma_2|$. Plot (c) displays $|\Theta_1|^2, \ldots, |\Theta_4|^2$. Plot (d) displays $|I(\mathbf{y},\mathbf{v})|$ at the true $\mathbf{v}$. The images are normalized to maximal value 1 and the colorbars are as in Fig. 5.

from $v_\perp - \Delta v_\perp/2$ to $v_\perp + \Delta v_\perp/2$ during the recording time window. We let $v_\perp = -V$ and $\Delta v_\perp = V$ to illustrate that even when the velocity variation $\Delta v_\perp$ is of the order of $v_\perp$, the position of the target is still well estimated (Fig. 11(b)). The velocity can be estimated as well (Fig. 11(c)): The corresponding singular vector is slightly perturbed from that in Fig. 5(c), but it still peaks at $u_\perp \approx v_\perp = -V$.

Robustness to strong additive noise (Figs. 12-13): We consider first data contaminated with 100% additive Gaussian white noise. By 100% we mean that the standard deviation of the noise equals the maximum of the modulus of the signals in the response matrix, in the frequency domain. The results shown in Fig. 12 are very robust to noise, as expected. The summation involved in the formation of the space-velocity imaging matrix averages out approximately the noise. It is only at very high levels of noise that this affects the results, as shown in Fig. 13 with 200% - and 300% -additive noise. One can observe that

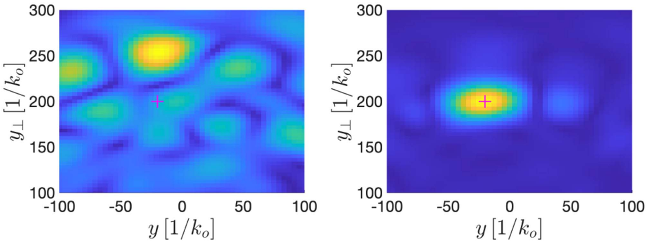

(a) Image from Γ_1 **(b) Image from Γ_2**

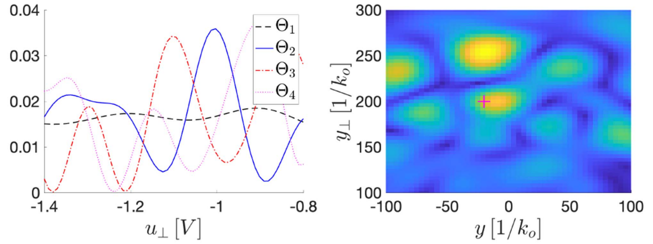

(c) Right singular vectors **(d) $|I(\mathbf{y},\mathbf{v})|$**

Fig. 11. Target acceleration: The configuration is as in Fig. 5, but the target has uniform acceleration so that its velocity increases linearly from $v_\perp - \Delta v_\perp/2$ to $v_\perp + \Delta v_\perp/2$ during data gather. Here $v_\perp = -V$, $\Delta v_\perp = V$ and $SCR = -9.8$ dB. Plots (a) and (b) display $|\Gamma_1|$ and $|\Gamma_2|$. Plot (c) displays $|\Theta_1|^2, \ldots, |\Theta_4|^2$. Plot (d) displays $|I(\mathbf{y},\mathbf{v})|$ at the true $\mathbf{v}$. The images are normalized to maximal value 1 and the colorbars are as in Fig. 5.

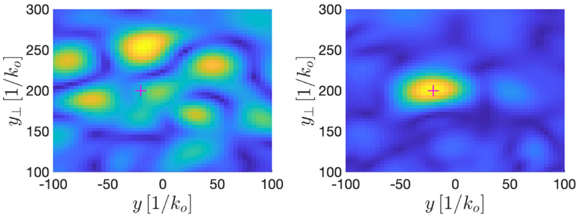

(a) Image from Γ_1 **(b) Image from Γ_2**

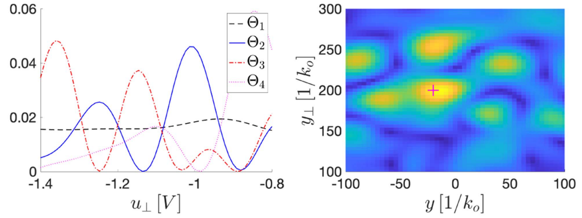

(c) Right singular vectors **(d) $|I(\mathbf{y},\mathbf{v})|$**

Fig. 12. 100% noise: Setup and plots as in Fig. 5, but the data are contaminated with Gaussian additive white noise. The first singular values are $(\sigma_j)_{j=1}^4 = (1.0608, 0.1977, 0.1223, 0.0962) \times 10^6$. Plots (a) and (b) display $|\Gamma_1|$ and $|\Gamma_2|$. Plot (c) displays $|\Theta_1|^2, \ldots, |\Theta_4|^2$. Plot (d) displays $|I(\mathbf{y},\mathbf{v})|$ at the true $\mathbf{v}$. The images are normalized to maximal value 1 and the colorbars are as in Fig. 5.

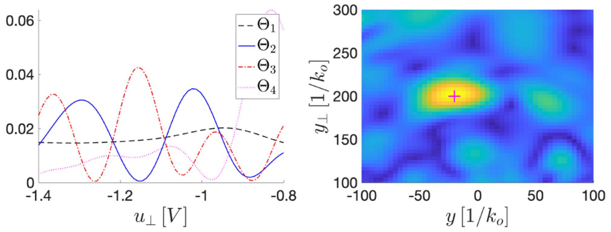

(a) Right singular vectors **(b) Image from Γ_2**

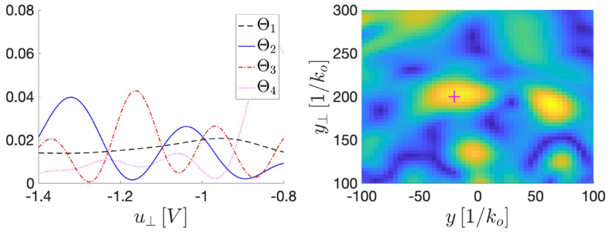

(c) Right singular vectors **(d) Image from Γ_2**

Fig. 13. 200% -additive noise (top) and 300% -additive noise (bottom). The right singular vector Θ_2 whose maximum is supposed to be at the target velocity $v_\perp = -V$ is slightly corrupted for 200% -additive noise (plot (a)) and strongly corrupted for 300% -additive noise (plot (c)). Similarly, the left singular vector Γ_2 is well centered at the target location $\mathbf{z} = (-20, 200)/k_o$ for 200% -additive noise (plot (b)) but it is strongly perturbed for 300% -additive noise (plot (d)). The first four singular values are $(\sigma_j)_{j=1}^4 = (1.2033, 0.3028, 0.2377, 0.1824) \times 10^6$ for 200% -noise and $(\sigma_j)_{j=1}^4 = (1.4066, 0.4249, 0.3480, 0.2669) \times 10^6$ for 300% -noise. The images (plots (b), (d)) are normalized to maximal value 1. The colorbars are the same as in Fig. 5.

the first and second singular values (coming from the stationary scenery and from the moving target, respectively) increase when the additive noise level increases. This is a manifestation of the level repulsion phenomenon that can be observed on random perturbations of low-rank matrices. This effect is described by random matrix theory [24], [31].

Robustness to motion in cross-range (Fig. 14): Here we present results for homogeneous clutter and a target that moves both in range and cross-range, with velocity $\mathbf{v} = (-1, -1)V$ (top plots) or $\mathbf{v} = (1, -1)V$ (bottom plots). In both cases we note that the target is imaged at the right location [Fig. 14(b),(d)], but there is a small bias in the estimation of the range velocity with the second left singular vector Θ_2 [Fig. 14(a),(c)]. We observe that this bias is a shift by an amount very close to the theoretical value given in (13).

A moving extended target (Fig. 15): The imaging method and analysis are not restricted to point targets. Recall that the data model (5), the expression (11) of the imaging function and the SVD analysis in section V consider a general reflectivity $\rho(\mathbf{x})$ of compact support. In Fig. 15, this support is the parallelogram drawn in red in plots (a), (b) and (c). The target is modeled by a reflectivity function that is constant in this support. The image obtained by our approach (plot (b)) peaks at the points of highest reflectance (corners of parallelogram). This is what a classical imaging function does for a stationary target, in weak or negligible clutter. Here the target moves, the clutter is not negligible and in addition to localizing the target, our method also gives its correct velocity (plot (c)).

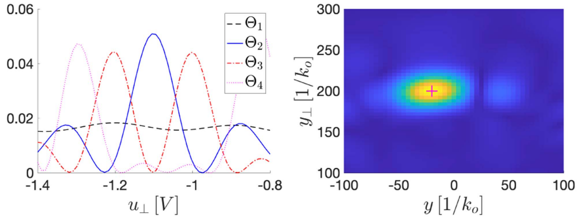

(a) Right singular vectors **(b) Image from Γ_2**

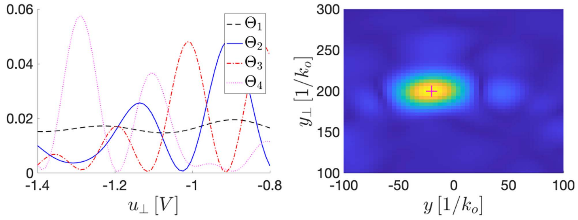

(c) Right singular vectors **(d) Image from Γ_2**

Fig. 14. Bias due to cross-range motion: The same configuration as in Fig. 5 but the target moves with velocity $\mathbf{v} = (-1, -1)V$ (top) and $\mathbf{v} = (1, -1)V$ (bottom). The right singular vector Θ_2 whose maximum should be at $v_\perp = -V$ is slightly shifted (plots (a), (c)) by an amount close to the theoretical value $\frac{z}{z_\perp} v = \pm 0.1V$ [see Eq. (13)]. The left singular vector Γ_2 is well centered at the true target location $\mathbf{z} = (-20, 200)/k_o$ (plots (b),(d)). The first four singular values are $(\sigma_j)_{j=1}^4 = (1.0071, 0.1348, 0.0415, 0.0231) \times 10^6$ for $\mathbf{v} = (-1, -1)V$ and $(\sigma_j)_{j=1}^4 = (1.0102, 0.1214, 0.0448, 0.0199) \times 10^6$ for $\mathbf{v} = (1, -1)V$. The images (plots (b), (d)) are normalized to maximal value 1. The colorbars are the same as in Fig. 5.

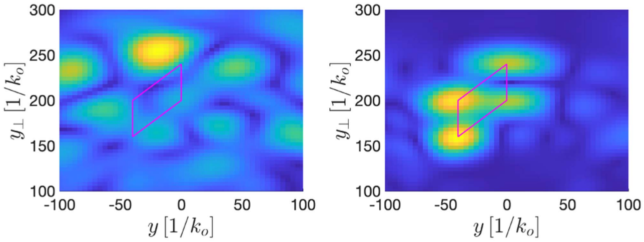

(a) Image from Γ_1 **(b) Image from Γ_2**

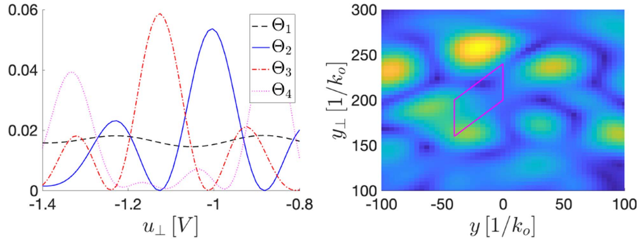

(c) Right singular vectors **(d) $|I(\mathbf{y}, \mathbf{v})|$**

Fig. 15. Extended target: The configuration is the same as in Fig. 5, but the target is extended and delimited by the red parallelogram. $SCR = -10$ dB. Plots (a) and (b) display $|\Gamma_1|$ and $|\Gamma_2|$. Plot (c) displays $|\Theta_1|^2, \ldots, |\Theta_4|^2$. Plot (d) displays $|I(\mathbf{y}, \mathbf{v})|$ at the true $\mathbf{v}$. The images are normalized to maximal value 1 and the colorbars are as in Fig. 5.

C. Two Moving Targets in Clutter

In Figs. 16 and 17 we show results for two moving targets in clutter. Both targets are point-like, with the reflectivity modeled by $\delta[\mathbf{x} - (\mathbf{z}_j + \mathbf{v}_j t)]$, where

$$\mathbf{z}_1 = (-20, 200)/k_o \quad \text{and} \quad \mathbf{z}_2 = (20, 160)/k_o,$$

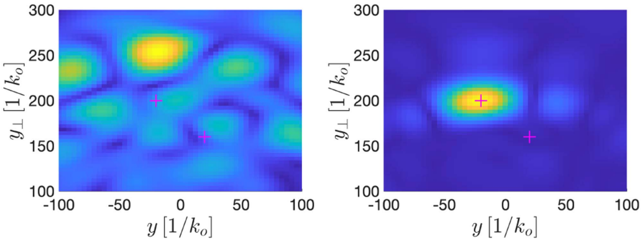

(a) Image from Γ_1 **(b) Image from Γ_2**

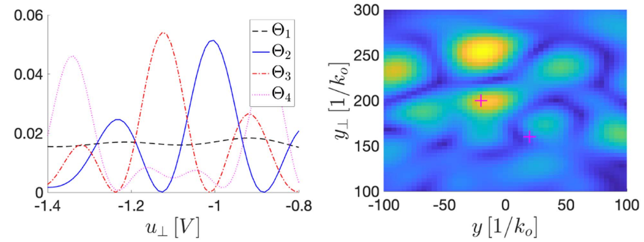

(c) Right singular vectors **(d) $|I(\mathbf{y}, \mathbf{v}_1)|$**

Fig. 16. Two targets with velocities $\mathbf{v}_1 = (0, -V)$ and $\mathbf{v}_2 = (0, 1.3V)$. Their locations at $t = 0$ are shown with red crosses. The search velocity interval is $[-1.4, -0.8]V$. First singular values are $(\sigma_j)_{j=1}^4 = (1.0072, 0.1298, 0.0319, 0.0215) \times 10^6$. Here $SCR = -6.8$ dB. Plots (a) and (b) display $|\Gamma_1|$ and $|\Gamma_2|$. Plot (c) displays $|\Theta_1|^2, \ldots, |\Theta_4|^2$. Plot (d) displays $|I(\mathbf{y}, \mathbf{v})|$ at $\mathbf{v} = \mathbf{v}_1$. The images are normalized to maximal value 1 and the colorbars are the same as in Fig. 5.

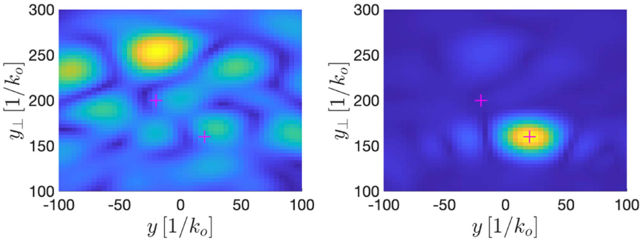

(a) Image from Γ_1 **(b) Image from Γ_2**

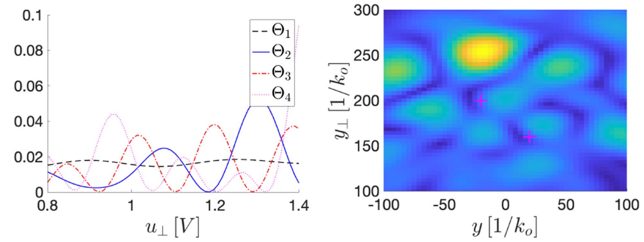

(c) Right singular vectors **(d) $|I(\mathbf{y}, \mathbf{v}_2)|$**

Fig. 17. Two moving targets, as in Fig. 16. First singular values: $(\sigma_j)_{j=1}^4 = (1.0138, 0.1134, 0.0331, 0.0214) \times 10^6$. Search velocity interval is $[0.8, 1.4]V$. Plots (a) and (b) display $|\Gamma_1|$ and $|\Gamma_2|$. Plot (c) displays $|\Theta_1|^2, \ldots, |\Theta_4|^2$. Plot (d) displays $|I(\mathbf{y}, \mathbf{v})|$ at $\mathbf{v} = \mathbf{v}_2$. Images are normalized to maximal value 1 and the colorbars are as in Fig. 5.

and

$$\mathbf{v}_1 = (0, -V) \quad \text{and} \quad \mathbf{v}_2 = (0, 1.3V).$$

The first target is clearly identified in Fig. 16, because the search velocity window $\mathbf{u} \in \{0\} \times [-1.4, -0.8]V$ contains $\mathbf{v}_1$. Again, due to the strong clutter, the correction to formula (11) plays a role and gives the largest singular value. The leading right singular vector Θ_1 does not display any peak in the search velocity window, so we can easily filter out the clutter effect, by ignoring the singular vector pair (Γ_1, Θ_1). The first moving target is captured by Θ_2, that peaks at the right velocity. The image of the target is captured by Γ_2 and it peaks at the correct location $\mathbf{z}_1$. The second target is not seen in Fig. 16, because its velocity is outside the search window. We can see it in Fig. 17, where $\mathbf{u} \in \{0\} \times [0.8, 1.4]V$. We identify there both the target velocity and its location using the singular vector pair (Γ_2, Θ_2).

In Figs. 16(d)-17(d) we plot the space-velocity imaging function computed at the true target velocities. These are the best images of the moving targets one could hope for, with an optimization approach without additional information or data. As we have seen in the previous section, because the clutter is strong, these images do a worse job in localizing the moving targets than our SVD approach [see Figs. 16(b)-17(b)].

VII. SUMMARY AND DISCUSSION

We introduced a novel way of processing active array response data, for improved imaging of moving targets in a stationary complex scene (clutter). The processing results in an imaging function that depends on both the search position and velocity and is approximately a sum of terms that are separable in these variables. The sampling of this imaging function on a search grid gives a "space-velocity" imaging matrix that, due to the separable terms, can be analyzed with the SVD. We showed that the right singular vectors in this decomposition are useful for identifying moving targets whose velocity is contained in the search domain. The left singular vectors store the images of the locations of the targets.

We showed that the imaging method is robust to strong and heterogeneous clutter, to additive noise and to perturbations of the model of uniform motion of the targets. We also compared its performance to that of STAP, carried out in an ideal situation where the covariance matrix of the clutter response can be estimated accurately. The results show that our method performs as well as STAP, but it does not require additional training data to estimate the covariance. Moreover, the method is not sensitive to the complexity of the clutter statistics.

When it comes to clutter removal, our method has an advantage over those based on sparsity and tensor decompositions. These methods are either not equipped to handle very strong clutter or they incorporate some version of STAP. Typically, they also use more data than assumed in this paper.

The computational complexity of our method can be controlled by first segmenting (windowing) the spatial and velocity search domain and then imaging in one window at a time. In principle, the images for multiple windows could be organized in a tensor that can be analyzed with HOSVD. Tensors could also be relevant for imaging with two arrays. We explained that when using one array at a time, the data are sensitive mostly to the range velocity of the target. The second array gives another range direction and then, the target velocity can be obtained via simple geometry. However, the HOSVD is not uniquely defined, it does not have all the nice properties of the SVD, and its computation involves iterative optimization. Thus, one might be better off with using one space-velocity search window and one array at a time.

APPENDIX A

Here we give the details of the derivation of the formulas in Section IV. We use the continuum aperture approximation, which replaces the sums over the antenna indexes by integrals. This is, basically, a numerical quadrature rule. Instead of placing hard bounds on the domains of integration, we use a Gaussian apodization. This simplifies the calculation and amounts to replacing the double sum in (9) by

$$\frac{4}{N(N+2)}\sum_{s=N/4}^{3N/4-1}\sum_{r=3N/4-s}^{5N/4-s} \rightsquigarrow \iint_{\mathbb{R}^2} \frac{2dx_r dx_s}{\pi a^2} e^{-2\frac{x_s^2}{a^2}-2\frac{(x_r+x_s)^2}{a^2}},$$

where x_r and (x_r+x_s) now vary continuously in $\mathbb{R}$.

We use this approximation in the definition (9) of the imaging function. The integrand is determined by the data model (5) and the matched filter (7), and its phase is given by (8). Integrating in x_r and (x_r+x_s) we get

$$\begin{aligned}
I(\mathbf{y},\mathbf{u}) =& \frac{1}{64\pi^2 y_\perp^2}\left[1+\frac{k_o^2a^4(v-u)^2}{16y_\perp^2V^2}-\frac{ik_oa^2(v^2-u^2)}{2y_\perp V^2}\right]^{-\frac{1}{2}} \\
&\times \int_{\mathbb{R}^2} d\mathbf{z}\,\rho(\mathbf{z})\,F\left[\frac{2}{c}\left(y_\perp - z_\perp + \frac{y^2}{2y_\perp}-\frac{z^2}{2z_\perp}\right)\right] \\
&\times \exp\left\{-\frac{k_o^2a^2(z-y)^2}{8y_\perp^2}\frac{\left[1-\frac{ik_oa^2(v^2-u^2)}{2y_\perp V^2}\right]}{\left[1+\frac{k_o^2a^4(v-u)^2}{16y_\perp^2V^2}-\frac{ik_oa^2(v^2-u^2)}{2y_\perp V^2}\right]}\right\} \\
&\times \exp\left\{-\frac{k_o^2a^2\left[\frac{(v_\perp-u_\perp)}{V}+\frac{(zv-yu)}{y_\perp V}\right]^2}{2\left[1+\frac{k_o^2a^4(v-u)^2}{16y_\perp^2V^2}-\frac{ik_oa^2(v^2-u^2)}{2y_\perp V^2}\right]}\right\} \\
&\times \exp\left\{-\frac{ik_o^3a^4}{8y_\perp^2}\frac{(z-y)\frac{(v-u)}{V}\left[\frac{(v_\perp-u_\perp)}{V}+\frac{(zv-yu)}{y_\perp V}\right]}{\left[1+\frac{k_o^2a^4(v-u)^2}{16y_\perp^2V^2}-\frac{ik_oa^2(v^2-u^2)}{2y_\perp V^2}\right]}\right\} + \text{c.c.}
\end{aligned}$$

To obtain this expression we used the following technical lemma, proved at the end of this appendix.

Lemma 1: If the probing signal is of the form (2) and we have $B \ll \omega_o$, as assumed in (3), then

$$\frac{1}{2\pi}\int_{\mathbb{R}} d\omega\, e^{-i\omega t}|\hat{f}(\omega)|^2 = F(t) + \text{ c.c.}, \tag{18}$$

with F defined in Proposition 1.

To simplify $I(\mathbf{y},\mathbf{u})$ as in Proposition 1, we need to estimate the following terms:

$$T_1 = \frac{k_oa^2}{y_\perp}\frac{|v-y|}{V}, \tag{19}$$

$$T_2 = \frac{k_oa^2}{y_\perp}\frac{|v^2-y^2|}{V^2} = T_1\frac{(v+y)}{V}, \tag{20}$$

$$T_3 = \frac{|zv-yu|}{y_\perp V}, \tag{21}$$

$$T_4 = \frac{k_o^3a^4}{y_\perp^2}|z-y|\frac{|v-u|}{V}\frac{|v_\perp-u_\perp|}{V}. \tag{22}$$

Note that due to the first exponential in the expression of $I(\mathbf{y},\mathbf{u})$, we have a large imaging function for search points satisfying $\frac{k_oa}{y_\perp}|z-y| \sim 1$. Moreover, due to the second exponential and the paraxial scaling $|z|, |y| \ll y_\perp \sim L$, we have a large imaging function for search velocities satisfying $k_oa\frac{|v_\perp-u_\perp|}{V} \sim 1$. These observations and the assumption $|u|, |v| \sim V$, lead to the following estimates of (20) and (22)

$$T_2 \sim T_1 \quad \text{and} \quad T_4 \sim \frac{k_oa^2}{y_\perp}\frac{|v-u|}{V} = T_1.$$

For the term (21) we have

$$\begin{aligned}
T_3 &= \left|\frac{(z-y)v}{y_\perp V}+\frac{y(v-u)}{y_\perp V}\right| \le \frac{|z-y|}{y_\perp}\frac{|v|}{V}+\frac{|v-y|}{V}\frac{|y|}{y_\perp} \\
&\sim \frac{1}{k_oa}\frac{|v|}{V}+\frac{|v-y|}{V}\frac{|y|}{y_\perp} \ll 1,
\end{aligned}$$

because $1/[k_oa] \sim \lambda_o/a \ll 1$ and $|y| \ll y_\perp \sim L$.

The assumption in Proposition 1 says that T_1 and therefore T_2 and T_4 are negligible. Using this in the expression of $I(\mathbf{y},\mathbf{u})$, we obtain (11). If the assumption is not satisfied, we can estimate the bias in the imaging function by evaluating it at $\mathbf{u} = (0, u_\perp)$. We observe that the peaks of the imaging function remain at search points $\mathbf{y} = \mathbf{z}$, but the range velocity is estimated with the small bias $|zv|/[y_\perp V]$.

Note that the cross-range velocity v also leads to some oscillations near the peaks of $I(\mathbf{y},\mathbf{u})$ and an increase in the standard deviation of the exponentials. These effects depend on how large T_1 is, which in turn depends on the Fresnel number k_oa^2/L. If the Fresnel number is large, it is possible in principle to get an estimate of the cross-range speed by adjusting u until the image is better focused. We do not elaborate further on this point.

Proof of Lemma 1: We have from the definition of $\Phi(h)$ in Proposition 1 that

$$\Phi(h) = \frac{1}{2\pi}\int_{\mathbb{R}} dw\, e^{-iwh}|\hat{\varphi}(w)|^2.$$

Moreover, (2) gives

$$\hat{f}(\omega) = \hat{\varphi}\left(\frac{\omega-\omega_o}{B}\right) + \overline{\hat{\varphi}\left(-\frac{\omega+\omega_o}{B}\right)}.$$

Since $B \ll \omega_o$, the effective supports of these two terms do not overlap and we get that

$$\left|\hat{f}(\omega)\right|^2 = \left|\hat{\varphi}\left(\frac{\omega-\omega_o}{B}\right)\right|^2 + \left|\hat{\varphi}\left(-\frac{\omega+\omega_o}{B}\right)\right|^2.$$

Substituting this in the left side of (18) we get the result. ☐

APPENDIX B

In this appendix we show that it is possible to test whether a singular value and associated singular vectors correspond to a moving target or not. For this purpose, we form a new space-velocity imaging matrix $\mathbf{I}'$, by sampling the imaging function $I(\mathbf{y},(0,u_\perp))$ at points $\mathbf{y}$ in a sub-region $\Omega' \subset \Omega$. Then, we compute the SVD of $\mathbf{I}'$. If the target is real, the new left singular vector will give an image that is a zoomed version of the original one, obtained by sampling in the bigger domain Ω. If there is no target, then the new image will be different. An illustration is in Fig. 18, where we display the results for the stationary configuration in Fig. 3 and for the configuration in Fig. 5, where there is a single moving target.

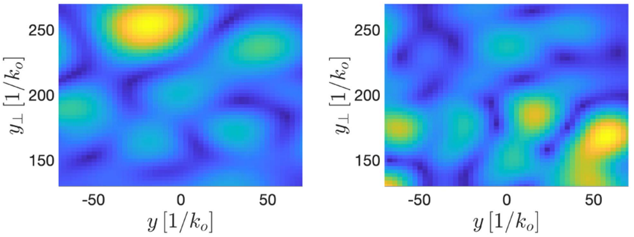

(a) Image from Γ_1 **(b) Image from Γ_2**

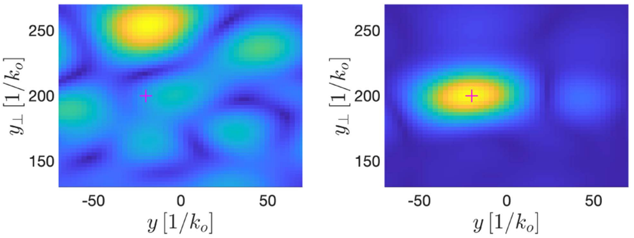

(c) Image from Γ_1 **(d) Image from Γ_2**

Fig. 18. Results in zoomed in region $\Omega' = [-70, 70]/k_o \times [130, 270]/k_o$. Top plots are for the configuration of Fig. 3. Plots (a)-(b): The images given by the first and second new left singular vectors. While plot (a) is a zoomed version of the plot in Fig. 3(a), the plot (b) is unrelated to the plot in Fig. 3(b). Bottom plots are for the configuration of Fig. 5. The images given by the first and second new left singular vectors are in plots (c) and (d). Plot (d) is a zoomed version of the plot of the target in Fig. 5(b). The images are normalized to maximal value 1. The colorbars are the same as in Fig. 5.

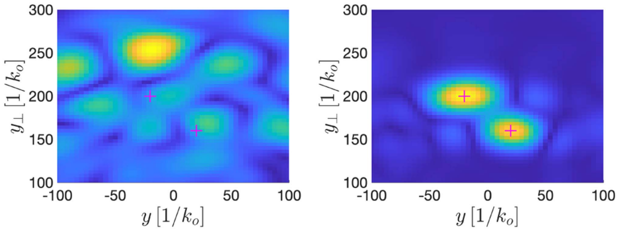

(a) Image from Γ_1 **(b) Image from Γ_2**

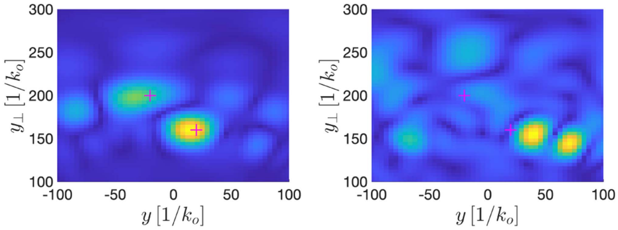

(c) Image from Γ_3 **(d) Image from Γ_4**

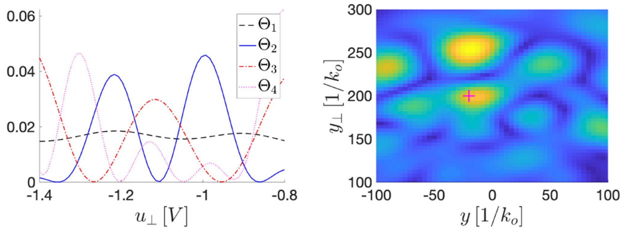

(e) Right singular vectors **(f) $|I(\mathbf{y}, \mathbf{v}_1)|$**

Fig. 19. Two moving targets with close velocities: Their locations at $t = 0$ are shown with red crosses and their velocities are $\mathbf{v}_1 = (0, -V)$ and $\mathbf{v}_2 = (0, -1.2V)$. The search velocity interval is $[-1.4, -0.8]V$. The images are normalized to maximal value 1. The colorbars are the same as in Fig. 5.

APPENDIX C

In this appendix and in Fig. 19 we consider a simulation with two moving targets that are not well separated in velocity. As mentioned in Section V, the second spectral pair (Γ_2, Θ_2) represents both targets. The right singular vector peaks around a value that is close to the velocities of the targets. The left singular vector peaks at the target locations. The third spectral pair (Γ_3, Θ_3) corresponds to a smaller singular value $\sigma_3/\sigma_2 \approx 0.45$. It is due to the corrections of the formula in Proposition 1 and we note that Γ_3 also peaks at the target locations. The fourth spectral pair, corresponding to $\sigma_4 \approx 0.18\sigma_2$ is not informative. The first four singular values are $(\sigma_j)_{j=1}^4 = (1.0210, 0.1603, 0.0734, 0.0301) \times 10^6$ and the $SCR = -6.8$ dB.

REFERENCES

[1] V. Anastassopoulos and G. A. Lampropoulos, "High resolution radar clutter classification," in *Proc. Int. Radar Conf.*, 1995, pp. 662–667.

[2] R. Baraniuk and P. Steeghs, "Compressive radar imaging," in *Proc. IEEE radar Conf.*, 2007, pp. 128–133.

[3] M. Ben Kilani, Y. Nijsure, G. Gagnon, G. Kaddoum, and F. Gagnon, "Cognitive waveform and receiver selection mechanism for multistatic radar," *IET Radar, Sonar Navigation*, vol. 10, pp. 417–425, 2016.

[4] S. Bernhardt, R. Boyer, S. Marcos, and P. Larzabal, "Compressed sensing with basis mismatch: Performance bounds and sparse-based estimator," *IEEE Trans. Signal Process.*, vol. 64, pp. 3483–3494, Jul. 2016.

[5] J. B. Billingsley, A. Farina, F. Gini, M. V. Greco, and L. Verrazzani, "Statistical analyses of measured radar ground clutter data," *IEEE Trans. Aerosp. Electron. Syst.*, vol. 35, pp. 579–593, Apr. 1999.

[6] L. Borcea, T. Callaghan, and G. Papanicolaou, "Synthetic aperture radar imaging and motion estimation via robust principal component analysis," *SIAM Imag. Sci.*, vol. 6, pp. 1445–1476, 2013.

[7] L. Borcea and J. Garnier, "Robust imaging with electromagnetic waves in noisy environments," *Inverse Problems*, vol. 32, 2016, Art. no. 105010.

[8] L. Borcea, G. Papanicolaou, and C. Tsogka, "Adaptive time-frequency detection and filtering for imaging in heavy clutter," *SIAM Imag. Sci.*, vol. 4, pp. 827–849, 2011.

[9] M. Born and E. Wolf, *Principles of Optics: Electromagnetic Theory of Propagation, Interference and Diffraction of Light*, Amsterdam, Netherlands: Elsevier, 2013.

[10] L. E. Brennan and L. S. Reed, "Theory of adaptive radar," *IEEE Trans. Aerosp. Electron. Syst.*, vol. AES-9, no. 2, pp. 237–252, Mar. 1973.

[11] L. E. Brennan and F. M. Staudaher, "Subclutter visibility demonstration," Tech. Rep. RL-TR-92-21, Adaptive Sensors Incorporated, 1992.

[12] F. Brigui, M. Boizard, G. Ginolhac, and F. Pascal, "New low-rank filters for MIMO-STAP based on an orthogonal tensorial decomposition," *IEEE Trans. Aerosp. Electron. Syst.*, vol. 54, no. 3, pp. 1208–1220, Jun. 2018.

[13] M. Çetin et al., "Sparsity-driven synthetic aperture radar imaging: Reconstruction, autofocusing, moving targets, and compressed sensing," *IEEE Signal Process. Mag.*, vol. 31, no. 4, pp. 27–40, Jul. 2014.

[14] H. Chen, F. Ahmad, S. Vorobyov, and F. Porikli, "Tensor decompositions in wireless communications and MIMO radar," *IEEE J. Sel. Topics Signal Process.*, vol. 15, no. 3, pp. 438–453, Apr. 2021.

[15] C. Y. Chen and P. P. Vaidyanathan, "MIMO radar spacetime adaptive processing and signal design," in *MIMO Radar Signal Processing*, J. Li and P. Stoica, Eds., Hoboken, NJ, USA: Wiley, 2009, pp. 235–281.

[16] M. Cheney and B. Borden, "Imaging moving targets from scattered waves," *Inverse Problems*, vol. 24, 2008, Art. no. 035005.

[17] M. Cheney and B. Borden, *Fundamentals of Radar Imaging*. Philadelphia, PA, USA: SIAM, 2009.

[18] M. Cheney and B. Borden, "Theory of waveform-diverse moving-target spotlight synthetic-aperture radar," *SIAM Imag. Sci.*, vol. 4, pp. 1180–1099, 2011.

[19] N. Cui, K. Xing, Z. Yu, and K. Duan, "Tensor-based sparse recovery space-time adaptive processing for large size data clutter suppression in airborne radar," *IEEE Trans. Aerosp. Electron. Syst.*, vol. 59, pp. 907–922, Apr. 2023.

[20] J. C. Curlander and R. N. McDonough, *Synthetic Aperture Radar*, New York, USA: Wiley, 1991.

[21] W. Feng, Y. Guo, Y. Zhang, and J. Gong, “Airborne radar space time adaptive processing based on atomic norm minimization,” *Signal Process.*, vol. 148, pp. 31–40, 2018.

[22] J. R. Fienup, “Detecting moving targets in SAR imagery by focusing,” *IEEE Trans. Aerosp. Electron. Syst.*, vol. 37, no. 3, pp. 794–809, Jul. 2001.

[23] J. Garnier and K. Solna, “Coherent interferometric imaging for synthetic aperture radar in the presence of noise,” *Inverse Problems*, vol. 24, 2008, Art. no. 055001.

[24] J. Garnier and K. Solna, “Applications of random matrix theory for sensor array imaging with measurement noise,” in *Random Matrix Theory, Interacting Particle Systems, and Integrable Systems*, P. Deift and P. Forrester, Eds., New York, NY, USA: Cambridge University Press, 2014, pp. 223–246.

[25] Q. He, N. H. Lehmann, R. S. Blum, and A. M. Haimovich, “MIMO radar moving target detection in homogeneous clutter,” *IEEE Trans. Aerosp. Electron. Syst.*, vol. 46, no. 3, pp. 1290–1301, Jul. 2010.

[26] M. Herman and T. Strohmer, “Compressed sensing radar,” in *Proc. IEEE Radar Conf.*, 2008, pp. 1509–1512.

[27] Z. Hu, W. Wang, and F. Dong, “MIMO radar accurate imaging and motion estimation for 3-D maneuvering ship target,” *IEEE Trans. Instrum. Meas.*, vol. 70, 2021, Art. no. 5503512.

[28] C. V. Jakowatz Jr, D. E. Wahl, and P. H. Eichel, “Refocus of constant-velocity moving targets in synthetic aperture radar imagery,” *Proc. SPIE*, vol. 3370, pp. 85–95, 1998.

[29] J. K. Jao, “Theory of synthetic aperture radar imaging of a moving target,” *IEEE Trans. Geosci. Remote Sens.*, vol. 39, no. 9, pp. 1984–1992, Sep. 2001.

[30] L. Jian and P. Stoica, *MIMO Radar Signal Processing*. Hoboken, NJ, USA: Wiley, 2008.

[31] I. M. Johnstone, “On the distribution of the largest Eigenvalue in principal components analysis,” *Ann. Statist.*, vol. 29, pp. 295–327, 2001.

[32] A. S. Khwaja, NÖ Önhon, and M. Cetin, “Compressed sensing methods for radar imaging in the presence of phase errors and moving objects,” in *Compressed Sensing in Radar Signal Processing*, A. M. De, Y. C. Eldar, and A. M Haimovich, Eds., Cambridge, MA, USA: Cambridge Univ. Press, 2019, pp. 321–353.

[33] T. G. Kolda and B. W. Bader, “Tensor decompositions and applications,” *SIAM Rev.*, vol. 51, pp. 455–500, 2009.

[34] H. Krim and M. Viberg, “Two decades of array signal processing research: The parametric approach,” *IEEE Signal Process. Mag.*, vol. 13, no. 4, pp. 67–94, Jul. 1996.

[35] M. Leibovich, G. Papanicolaou, and C. Tsogka, “Synthetic aperture imaging and motion estimation using tensor methods,” *SIAM Imag. Sci.*, vol. 13, pp. 2213–2249, 2020.

[36] X. Ming, D. Vu, L. Xu, J. Li, and P. Stoica, “On MIMO radar transmission schemes for ground moving target indication,” in *Proc. Conf. Rec. 43rd Asilomar Conf. Signals, Syst. Comput.*, 2009, pp. 1171–1175.

[37] NÖ Önhon and M. Cetin, “SAR moving target imaging in a sparsity-driven framework,” *Proc. SPIE*, vol. 8138, pp. 23–31, 2011.

[38] D. J. Rabideau and A. Steinhardt, “Improved adaptive clutter cancellation through data-adaptive training,” *IEEE Trans. Aerosp. Electron. Syst.*, vol. 35, no. 3, pp. 879–891, Jul. 1999.

[39] I. S. Reed, J. D. Mallett, and L. E. Brennan, “Rapid convergence rate in adaptive arrays,” *IEEE Trans. Aerosp. Electron. Syst.*, vol. 6, pp. 853–863, 2007.

[40] D. A. Shnidman, “Generalized radar clutter model,” *IEEE Trans. Aerosp. Electron. Syst.*, vol. 35, no. 3, pp. 857–865, Jul. 1999.

[41] A. Soĝanlı and M. Çetin, “Low-rank sparse matrix decomposition for sparsity-driven SAR image reconstruction,” in *Proc. 3rd Int. Workshop Compressed Sens. Theory Appl. Radar, Sonar Remote Sens.*, pp. 239–243.

[42] G. W. Stimson, H. D. Griffits, C. J. Baker, and D. Adamy, *Introduction to Airborne Radar*, 3rd ed., Edison, New York, NY, USA, Scitech Publishing, 2014.

[43] P. Stoica and A. Nehorai, “MUSIC, maximum likelihood, and Cramer-Rao bound,” *IEEE Trans. Acoust., Speech, Signal Process.*, vol. 37, no. 5, pp. 720–741, May 1989.

[44] I. Stojanovic and W. C. Karl, “Imaging of moving targets with multi-static SAR using an overcomplete dictionary,” *IEEE J. Sel. Topics Signal Process.*, vol. 4, pp. 164–176, Feb. 2010.

[45] B. Tang, J. Tang, and Y. Peng, “Detection of heterogeneous samples based on loaded generalized inner product method,” *Digit. Signal Process.*, vol. 22, no. 4, pp. 605–613, 2012.

[46] S. Torquato and F. H. Stillinger, “Local density fluctuations, hyperuniformity, and order metrics,” *Phys. Rev. E.*, vol. 68, 2003, Art. no. 041113.

[47] P. B. Tuuk, “Clutter rejection and adaptive filtering in compressed sensing radar,” in *Compressed sensing in radar signal processing*, A. De Maio, Y. C. Eldar, and A. M. Haimovich, Eds., Cambridge, U.K.: Cambridge Univ. Press 2019, pp. 49–71.

[48] X. Wang, W. Wang, J. Liu, Q. Liu, and B. Wang, “Tensor-based real-valued subspace approach for angle estimation in bistatic MIMO radar with unknown mutual coupling,” *Signal Process.*, vol. 116, pp. 152–158, 2015.

[49] B. Xu, X. Lu, H. Gu, and W. Su, “Tensor structure-based ground clutter suppression approaches for pulse doppler radar,” *Remote Sens. Lett.*, vol. 15, pp. 457–465, 2024.

[50] Z. Yang, X. Li, H. Wang, and W. Jiang, “On Clutter Sparsity Analysis in Space-Time Adaptive Processing Airborne Radar,” *IEEE Geosci. Remote Sens. Lett.*, vol. 10, no. 5, pp. 1214–1218, Sep. 2013.

[51] M. Yasin, M. Çetin, and A. S. Khwaja, “SAR imaging of moving targets by subaperture based low-rank and sparse decomposition,” in *Proc. 25th Signal Process. Commun. Appl. Conf.*, 2017, pp. 1–4.

[52] X. Yi, S. Zhang, and Y. Zhou, “Efficient 2-D MUSIC algorithm for super-resolution moving target tracking based on an FMCW radar,” *Geodesy Geodynamics*, vol. 15, pp. 504–515, 2024.

[53] X. Zhang, T. Wang, W. Cui, and D. Wang, “A novel clutter suppression algorithm for airborne radar via subspace projection,” *IEEE Sensors J.*, vol. 25, no. 1, pp. 962–970, Jan. 2025.

Liliana Borcea has been a Professor of applied mathematics since 1996: First with Rice University, where she rose in rank to Noah Harding Professor in 2007. She was with the University of Michigan as a Peter Field Collegiate Professor from 2013 to 2024 and has been with Columbia University as George P. Livanos Professor since 2024. She was a Rothschild Distinguished Visiting Fellow with the Isaac Newton Institute of Mathematical Sciences, Cambridge University, U.K., in 2023. Her research interests include inverse problems, with particular focus on inverse scattering in complex and heterogeneous media. She was the recipient of the AWM-SIAM Sonia Kovalevsky Prize in 2017. Became a SIAM Fellow in 2018. She was the Editor in Chief of the SIAM Journal of Multiscale Modeling and Simulations (2020-2025). She was elected to the American Academy of Arts and Sciences in 2023.

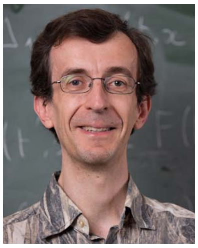

Josselin Garnier has been a Professor of applied mathematics, since 2001, first in Toulouse, then in Paris with Université Paris Diderot and Ecole Normale Supérieure, and finally with Ecole Polytechnique, since 2016. He has been the Head of the Department of Applied Mathematics, Ecole Polytechnique, since 2023. He has authored three hundred papers in his research interests which include the interface of probability theory and analysis, concerns the modeling and study of random phenomena, in particular wave propagation and imaging in complex media, the quantification of uncertainties in numerical simulation, and stochastic algorithms, and has written five research books and three textbooks. He was the recipient of the Blaise Pascal Prize in 2007 and the Felix Klein Prize in 2008. He was an Invited Speaker with the International Congress of Mathematicians in 2018. In 2023, he was elected a member of the French Academy of Sciences.